Microscopic Simulation of GEM Signals

von

Moritz Seidel

Bachelorarbeit in Physik

vorgelegt der

Fakultät für Mathematik, Informatik und Naturwissenschaften
der RWTH Aachen

angefertigt im

III. Physikalischen Institut A

bei

Prof. Dr. Thomas Hebbeker

Zweitgutachter

Prof. Dr. Christopher Wiebusch

August 2018

Contents

List of Figures

Chapter 1

Introduction

One of the first major inventions in particle physics detector studies was the Cloud Chamber by Wilson in 1911. Only one year later, Hans Geiger developed a detector based on the same principle as the Gas Electron Multipliers (GEMs) studied in this thesis, which was later upgraded to the famous Geiger-Müller counter in 1928 [3]. GEMs are commonly used to detect muons, a particle discovered in 1936 by Carl D. Anderson and Seth Neddermeyer while studying the decay of cosmic rays.

While the Geiger-Müller counter is only capable of measuring the number of ionizing particles, a very similar kind of detector, the proportional counter, was invented later, which is also capable of measuring the particle energy.

These particle detectors have been continuously improved to this day to achieve better performance of the detectors or to make them more compact.

In 1980, the Micro Pattern Gas Detectors (MPGD) were established. They are able to achieve great charge amplification with microscopic structures together with a fast ion collection and thus provide improved performance at high particle rates.

One of these MPDGs is the GEM, which was invented in 1997 by Fabio Sauli[2]. GEMs have several advantages compared to other detectors such as being able to achieve great amplification on very small scales and are thus optimally suited as detectors in settings where space is limited. Another great advantage is that they can be produced and operated in any desired geometry which leads to a high usage flexibility of the detectors. As will be discussed later, these detectors consist of one or more GEM foils (typically three foils are used) which also results in a high customization potential of the detector.

The goal of this thesis is to simulate the behavior and the performance of GEM detectors using the simulation toolkit `Garfield++` [7] to better understand the influence of factors such as gas composition, geometry and environmental parameters on the detectors.

1.1 Applications of GEM detectors

GEM detectors have been and are used in many experiments with great success.
COMPASS was the pioneering experiment for GEM technology usage in large particle physics experiments. It employed 22 GEM detectors with an active area of 10×10 cm^2 from 2000-2007.
STAR started operating 24 medium-sized triple-GEM detectors in the forward region of its detector. The GEM foils were shaped as circular quadrants with an outer diameter of 38 cm and an inner radius of 9.5 cm. [22]
At CERN, **TOTEM** utilizes 20 medium-sized triple-GEM detectors of a semi-circular shape, while **LHCb** employs 12 pairs of triple-GEM detectors in the immediate proximity of the beam pipe where they sustain rates of up to 500 kHz cm^{-2}[1].
The **CMS** [19] GEM project [1] represents the next step in the evolution of GEM detectors as it will use a large number of large-size detectors with an active area of 0.345 m^2 for the short chambers and 0.409 m^2 for the long chambers as opposed to the previously used medium-sized detectors. The production of these large-size GEMs has not been done previously and a new production process has been developed during the CMS GEM project.
The design of the GEM detectors for CMS outlined in [1] serves as a starting point for the simulation of the signals in GEMs in this thesis.

Chapter 2

GEM Detectors

2.1 Design

The central components of a GEM detector are the GEM foils. These foils are usually made of a 50 µm thick non-conductive Kapton[1] foil, coated with a 5 µm copper layer on each side.
Small double-conical holes are etched into the foils, with an outer diameter of about 70 µm and an inner diameter of about 50 µm. The holes typically have a pitch of 140 µm and are arranged in a hexagonal pattern.
In figure 2.1, the cross section of a double mask hole (i.e. etching performed from both sides) is shown.
If multiple foils are used, the distance between the foils is typically on the order of 1-2 mm. In addition, a drift cathode is installed above the foil (stack) and an anode is installed at the bottom. The anode is typically divided into small strips which serve as the readout of the chamber.
Increasing high voltage (HV) is applied to the cathode (most negative HV), upper

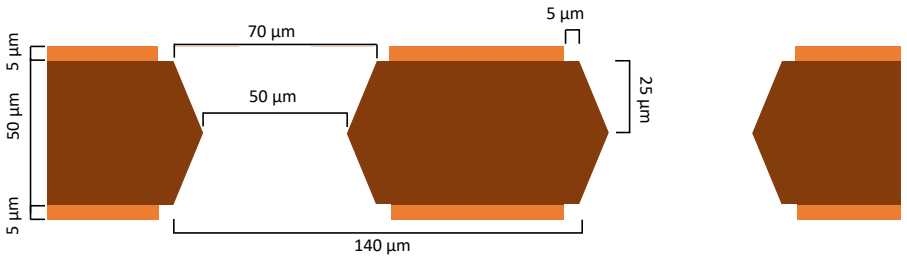

Figure 2.1: Sketch of a GEM foil produced with the double mask process as outlined in [1].

[1] A polyimide foil developed by DuPont in the 1960s

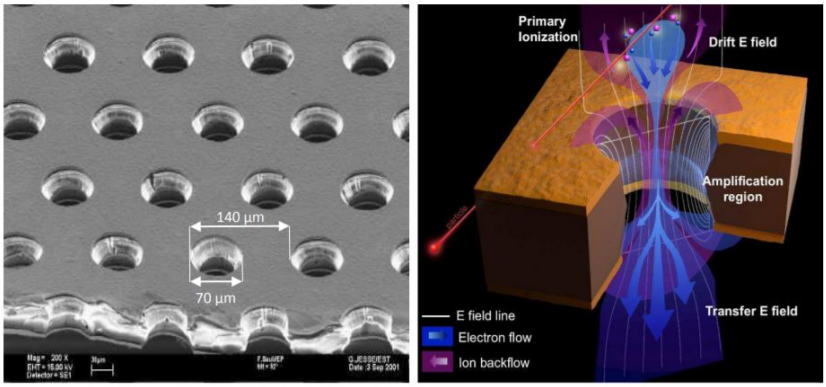

Figure 2.2: Scanning electron microscope picture of a double mask GEM foil (left). Schematic view of the electric field lines (white), electron flow (blue), and ion flow (purple) through a bi-conical GEM hole (right). Taken from [1].

and lower sides of the foils, and the anode (most positive HV). This is either done by a single channel HV-supply and a resistive voltage divider or by a multi channel supply. The multi channel HV-supply allows for different configurations of the detectors' electric fields as each applied voltage can be varied individually.
The chamber volume is filled with a counting-gas mixture. Common choices are mixtures of Ar/CO_2 or $Ar/CO_2/CF_4$. Eco-unfriendly gases such as CF_4 should be avoided if other gases achieve similar performance.
In figure 2.2 a Scanning electron microscope picture of a double mask GEM foil

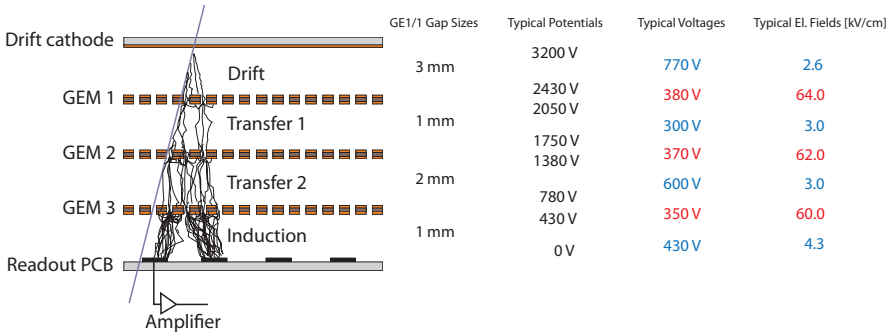

Figure 2.3: Principle of operation of the triple layer GE1/1 GEM chamber and definition of drift, transfer, and signal induction gap regions within the detector. The columns on the right list the actual gap sizes in GE1/1, typical operation values for the electric potentials at the eight electrodes and electric field strengths inside the holes (red) and inside the drift, transfer and induction regions (blue). Taken from [1].

can be seen. These GEMs will be installed in the CMS experiment at CERN according to the configuration shown in figure 2.3 (a spacing between cathode, foils and anode of 3-2-1-2 mm and a most negative potential of 3200 V) during the Long Shutdown 2 in 2019-2020.
The setup of the GE1/1 detector as outlined in [1] is the starting point for this thesis and is used as default configuration in most cases. It is fundamental to analyze its characteristics in detail as it will be used for muon detection and triggering purposes in the experiment for many years.

2.2 Working principle

In general, gaseous detectors have different working regions as shown in figure 2.4. At low voltages the electron and ion recombine before they can drift apart from each other. When the electric field strength is increased (corresponding to an increased voltage), the electrons undergo avalanche multiplication. The collected charge in this working region is proportional to the initial number of created electron-ion pairs.
At very high field strengths, the proportionality is lost and in the Geiger-Müller region every produced charge produces an identical signal due to a continuous

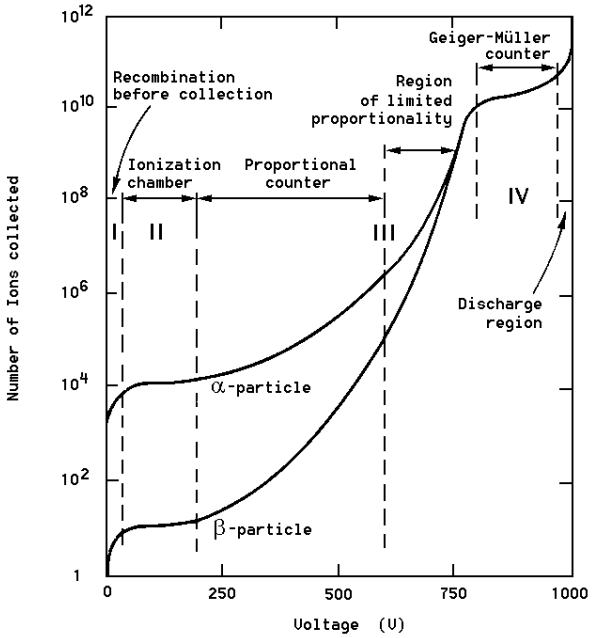

Figure 2.4: Collected charge for different working voltages. Working regions are labeled. The curves are α-particles and β-particles (electrons).[23]

avalanche. For even higher electric fields a continuous discharge takes place inside the detector even without a signal. This should be avoided because it can damage the detector.

A GEM detector is based on this principle of ionization and gas amplification and belongs to the category of proportional counters. When an ionizing particle, e.g. a muon, passes through the chamber, it ionizes some of the gas atoms, producing a negatively charged electron (e^-) and a positively charged ion (eg. Ar^+). The electrons travel towards the anode, while the ions travel towards the cathode, both driven by the applied electric field.

In GEMs, the electrons that are directly produced by an ionization due to the passing ionizing particle are named primary electrons. These primary electrons can have energies as high as 200 eV and are often capable of ionizing other atoms right away. The electrons produced by this mechanism are called secondary electrons.

If an electron reaches one of the foils and enters into a hole, it is accelerated rapidly in the high electric field of the hole which reaches up to $60\,\mathrm{kV\,cm^{-1}}$ and thus becomes able of ionizing more gas atoms inside the hole creating an avalanche process inside the holes. The electrons that are produced inside the holes of the foils are called avalanche electrons.

This avalanche process leads to a great amplification of the produced primary and secondary electrons and is amplified exponentially when more foils are used. The goal is to produce enough electrons so that a signal can be detected by the readout strips and the induced charge can be measured by the readout electronics, but not to produce a charge that can damage the detector.

The simulated GEM detector is filled with a gas mixture of Ar/CO_2. Argon is used as counting-gas and carbon dioxide as quenching gas. The quenching gas is necessary because an excited ion can emit a UV photon which could trigger another avalanche due to the photo-electric effect. Since argon is a single atom particle, it can not absorb the excited energy and will emit this photon. The CO_2, since it has more degrees of freedom, can absorb the photon and dissipate the energy via inelastic collisions within the molecule. Electrons also directly attach to the CO_2 and thus the fraction of CO_2 determines the gain of the chamber. The default gas mixture in the CMS GEM detectors is 70% Ar and 30% CO_2.

2.3 Important parameters

Some important parameters describing the performance of the GEM detector are listed here. They can be optimized to yield a better amplification and performance.

Gain: One of the most important parameters to describe an amplification detector

is the gain. The gain can be defined as

$$G = \frac{N_{R.e.}}{N_{p.e.}}, \tag{2.1}$$

where $N_{R.e.}$ is the number of electrons that hit the readout plane and $N_{p.e.}$ is the number of primary electrons. If the gain is higher, the signal can more clearly be separated from noise, leading to a higher detection efficiency.

Transparency: Not all electrons that are produced by the ionizing particle or in the avalanche process reach the readout strips.
Some do not reach a hole and therefore do not start the avalanche process at all, they just stick to the top of the foils. Others might stick to the bottom of the foils after exiting the hole. This will be discussed in more detail in the analysis section.
The primary transparency (T_p) and foil transparency (T_f) can be defined as

$$T_p = \frac{N_{p.h.} + N_{s.h.}}{N_{p.e.} + N_{s.e.}}, \tag{2.2}$$

$$T_f = \frac{N_{R.e.}}{N_{tot}}, \tag{2.3}$$

where $N_{p.h.}$ and $N_{s.h}$ represent the primary and the secondary electrons that reach a hole, respectively. $N_{p.e.}$ and $N_{s.e.}$ is the number of produced primary and secondary electrons. N_{tot} is the total amount of electrons produced in the avalanche process. For a multiple foil stack the foil transparency describes the fraction of electrons reaching the next foil over the electrons produced in the foil above.
It is desirable to maximize the primary transparency and the foil transparency. It will be analyzed how the geometry and high voltage distribution can be modified to achieve better transparencies.

Temporal and spacial distribution: The temporal distribution can be split into two parameters.
The first parameter is the time between the initial ionization by the muon and the arrival of the electrons on the readout plane. This may be expected to be largely dependent on the drift velocity of the gas mixture used in the detector.
The second parameter is the time interval over which the electrons are spread out at the readout plane. This needs to be minimized if many hits are expected within a short time window to be able to separate different events in the same readout strips.
The spacial spread of the electrons on the readout board belonging to the same avalanche is also important. If many signals are expected to hit a detector at the same time, a small spread of the signal at the readout board is important so that signals close to each other can be distinguished clearly.

Ion Backdrift: In each ionization, not only an electron is produced, but also an ion, which drifts towards the cathode. As ions are much heavier than electrons, the acceleration of the ions due to the electric field is small compared to the electrons and thus the ions are not expected to cause any ionizations inside the chamber.

Discharge: Due to dust particles in the detector or sharp edges of metal inside the strong electric field, spontaneous discharges can occur, producing a large number of electrons. This either creates a false signal that needs to be identified and discarded or can even damage the detector significantly. As this thesis represents an idealized simulation, discharges are not considered. However, they have to be kept in mind when interpreting the results of the simulation.

In this thesis, the gain, the primary transparency and the foil transparency as well as the temporal and spacial resolution are investigated and discussed.

Chapter 3

Simulation

In this chapter the simulation process will be outlined, starting with the geometry and field calculation and concluding with the avalanche simulation.

3.1 Geometry and fields

The geometry of the detector describes parameters like the number of foils, spacing of the foils, spacing size and shape of the holes.
For this part the program `Ansys 16.1`[6] is chosen. `Ansys` offers the functionality to be operated by its own scripting language. This is beneficial because some parameters can be changed quickly afterwards this way. It also runs on the CERN Batch system via `ansbatch`, which was also used.
Another great advantage of `Ansys` is that it is able to compute the electric fields needed for the detector.
The script to simulate geometry and fields is based on the slides of the RD51 simulation school 2011[4].
First the characteristics of the elements used in the construction are defined. To simulate the GEM foils, only two quarter-holes have to be created. This is shown in figure 3.1. For a GEM stack, multiple of these segments are created on top of each other with the desired spacing. To achieve a correct simulation of the geometry, and most importantly, the electric fields at all points in the mirrored foil, boundary conditions have to be set next. For the copper layers, an applied constant potential is defined. Finally, the meshing is done and the geometry and electric field maps are computed and stored. Figure 3.2 shows the electric field with a single foil configuration as simulated by `Ansys`.
Further details regarding the finite element method used by `Ansys` can be found in [5].

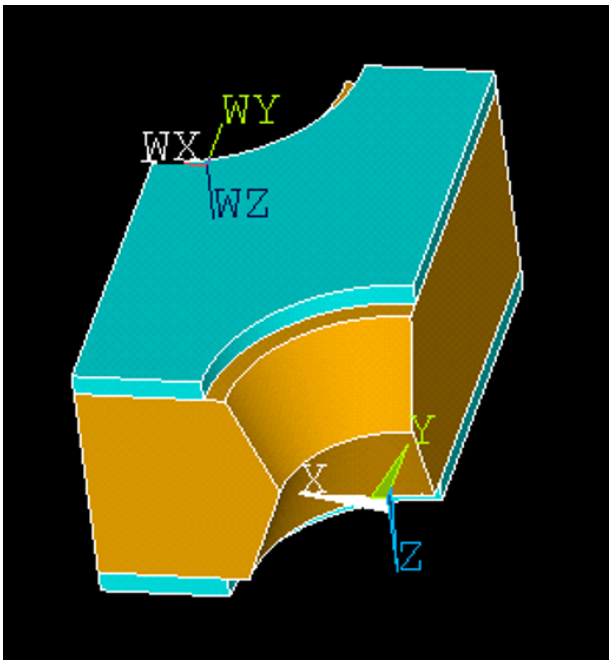

Figure 3.1: Simulated foil segment with conical cutouts. Kapton (50 µm thick) in orange and copper (5 µm on both sides) in blue.

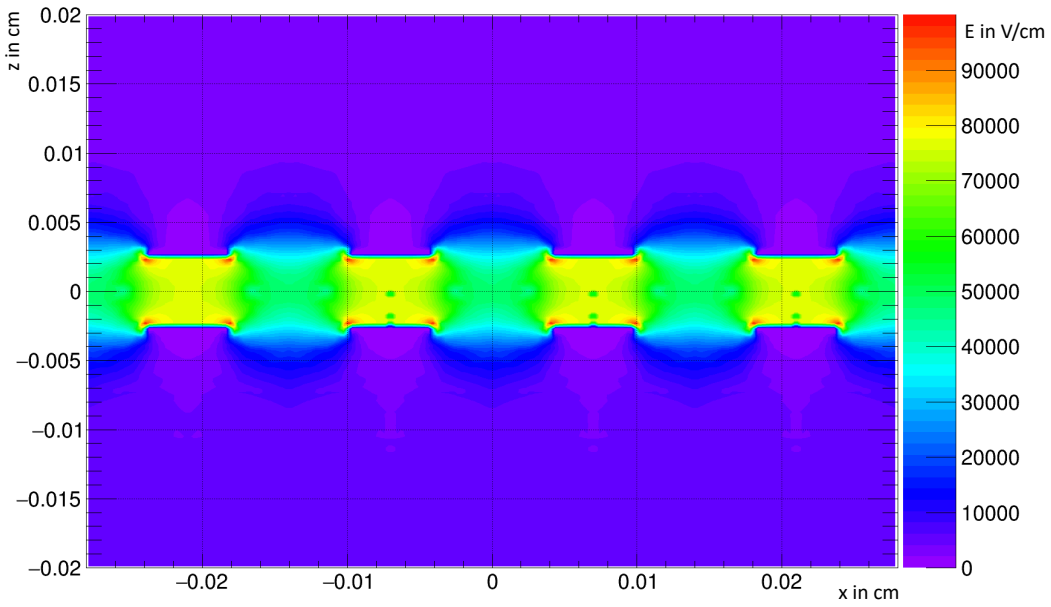

Figure 3.2: Electric field of a single GEM foil simulated with `Ansys`. Electric field inside the holes (greens regions) is up to 60 kV/cm and in the drift regions around 5 kV/cm

3.2 Avalanche computing

The avalanche computation is done with the `Garfield++` toolkit. `Garfield++` is a reimplementation of the Fortran framework `Garfield` in C++. The authors describe `Garfield++` as "a toolkit for the detailed simulation of particle detectors that use gas and semi-conductors as sensitive medium" [7].

To run the simulation with `Garfield++`, first the files generated by `Ansys` are read in. The geometry as well as the field are mirrored in the program so that (theoretically) an infinite foil or chamber can be simulated.

Because the simulation of an infinite chamber would be impractical, a *sensor* is defined in the program. This *sensor* is the area in which the avalanche is expected to take place. Real experiments show that signals are spread up to a maximum of 1 mm in the x and y direction [10]. To be safe a *sensor* area of 2 mm in x and y direction is chosen to be simulated over the whole GEM stack.

Consecutively, the gas mixture is specified and some environmental variables are supplied. Using the `Magboltz` [8] interface in `Garfield++` nearly arbitrary gas mixtures of up to six gases can be modelled.

At this point, either a single primary electron or an ionizing particle passing through the gas volume can be simulated.

3.2.1 Single electron simulation

To initiate a single electron avalanche, an electron is placed at a point inside an ionizable gas mixture within the defined *sensor* area. To this primary electron an initial momentum as well an initial energy and starting time are assigned.

From here on, the microscopic avalanche process can progress. The microscopic avalanche computes every time and distance step of the electron individually. It also computes all of the avalanche electrons produced inside the foil holes. The program provides an option to run a less accurate fast simulation which is not investigated in this thesis. This fast simulation has to be used for the simulation of the ion drift since `Garfield++` is not (yet) able to simulate them fully, for example an ion can not trigger another avalanche, but this is not relevant as noted above and the ions are not addressed in detail in this thesis.

As output of the avalanche computation, the program returns all previously mentioned parameters at the start and endpoints of the initial and the produced electrons and also tracks the produced ions. All intermediate points of a specific electron are recorded as well.

In figure 3.3 an example of a typical avalanche is shown. It can clearly be seen that the ionizations only take place inside the foil holes.

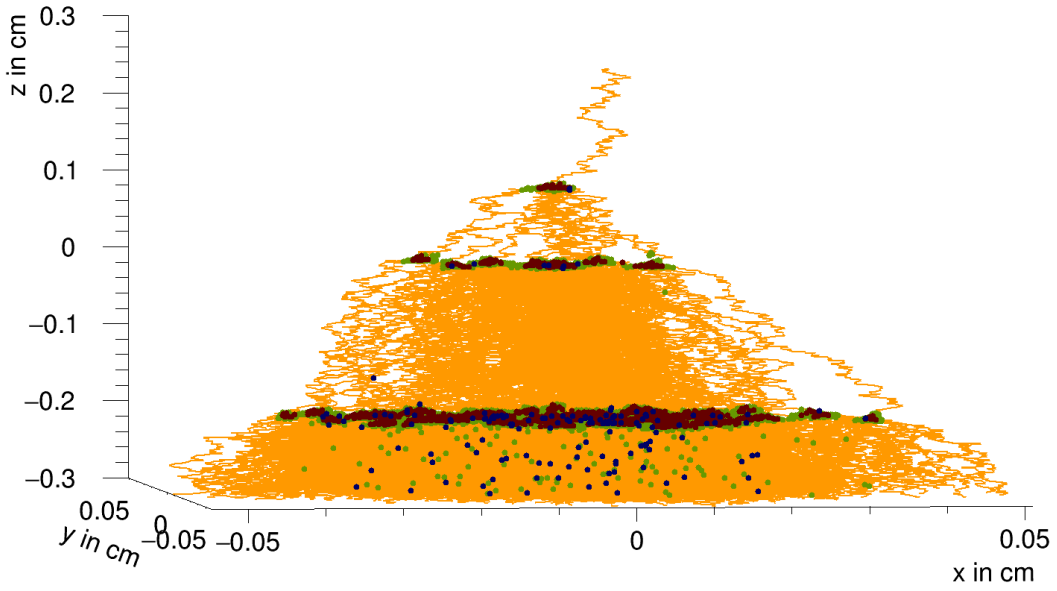

Figure 3.3: Single electron avalanche in a triple layer GEM stack setup. Drift lines (orange), ionization (brown), excitement (green) and electron capture (blue) are shown. GEM foils located at z = 0.1 cm, z = 0.0 cm and z = -0.2 cm. Primary electron starting point at z = 0.25 cm and readout plane at z = -0.3 cm

3.2.2 Ionizing particle simulation

To simulate an ionizing particle, the interface with `Heed` [9] is used. Using `Heed`, many different ionizing particles can be simulated; this thesis focuses on muons.

First the type, energy and path of the particle through the detector are defined.

A short simulation is run to determine the starting parameters of the produced primary electrons in the detector.

The primary ionizations take place in so called *clusters*. These *clusters* may consist of multiple electrons, because some primary electrons possess more kinetic energy than the ionization potential of the atoms in the gas mixture. Thus these electrons can directly ionize another atom. This is called secondary ionization.

There are two ways secondary ionizations can be treated in the simulation. One way is to let the program compute these secondary ionizations together with the primary ionizations. For this, "enable δ electron transport" has to be enabled. This will use the internal δ transport algorithm of `Heed`.

Using this option, the secondary electrons are directly returned in the same *cluster* together with the initial primary electron. The downside of this option is that the internal δ transport of `Heed` does not compute the final (kinetic) energies of the primary and secondary electrons.

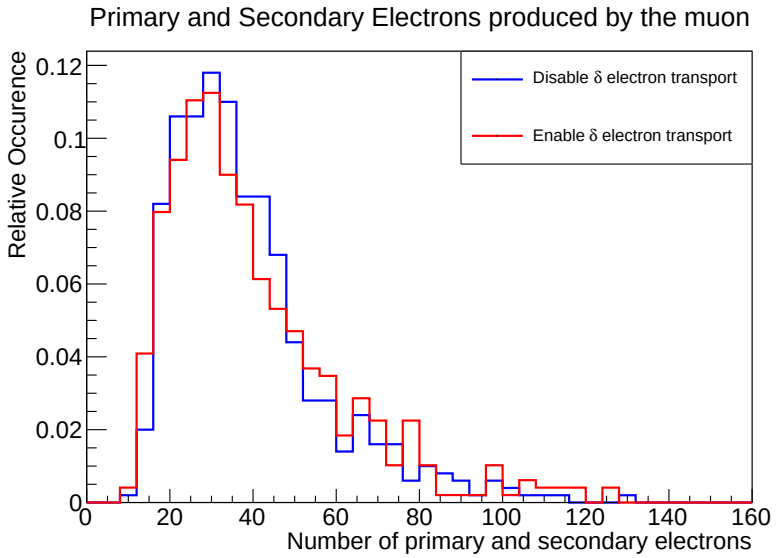

Figure 3.4: Comparing the number of primary and secondary electrons for enabled (red) and disabled (blue) δ electron transport setting in `Heed` at muon energy of 1 GeV.

The other method, which yields a more precise simulation of the initial electrons, is to "disable δ electron transport". When disabled, the *clusters* will only consist of the primary electron. Furthermore, the information about the (kinetic) energy of this primary electron is now known. When placing this primary electron inside the chamber, it will immediately produce secondary ionizations and thus secondary electrons are simulated by `Garfield++`. But, in this setting, the energies of the secondary electrons are also known as the secondary ionization takes place in the main avalanche.
To be sure that both techniques produce comparable results, the number of electrons produced is compared in figure 3.4.
Even though the number of produced primary electrons is the same as the ones calculated and observed in experiments ([20]), the number of produced secondary electrons in this simulation (with both enabled and disabled δ electron transport) is less by a factor of tree than the number of secondary electrons observed in experiments and presented in [20]. It has been tried to correct this by a manual calculation of the Townsend coefficient in the program, which produced the same results and thus the cause of this factor is still unknown. The cross sections from the `Magboltz` database will be used for all simulations.
Since there is no difference in the number of electrons, the more precise second method will be used from here on because it renders more information.
The starting location, the energy, the momentum and time of all primary electrons

are stored in a vector and are then used for starting the avalanche process. This follows the same logic as the single electron simulation presented in 3.2.1.
In figure 3.5 a typical avalanche produced by a muon is shown. Many ionizations inside the holes can be seen, but also some secondary ionizations along the muon path. Again, the three layers of the GEM can be clearly distinguished and it becomes evident that the avalanche process only takes place inside the holes. Due to the large number of electrons inside the last induction gap, a high number of dissociative electron capture by molecules and excitation of molecules without ionization take place here.

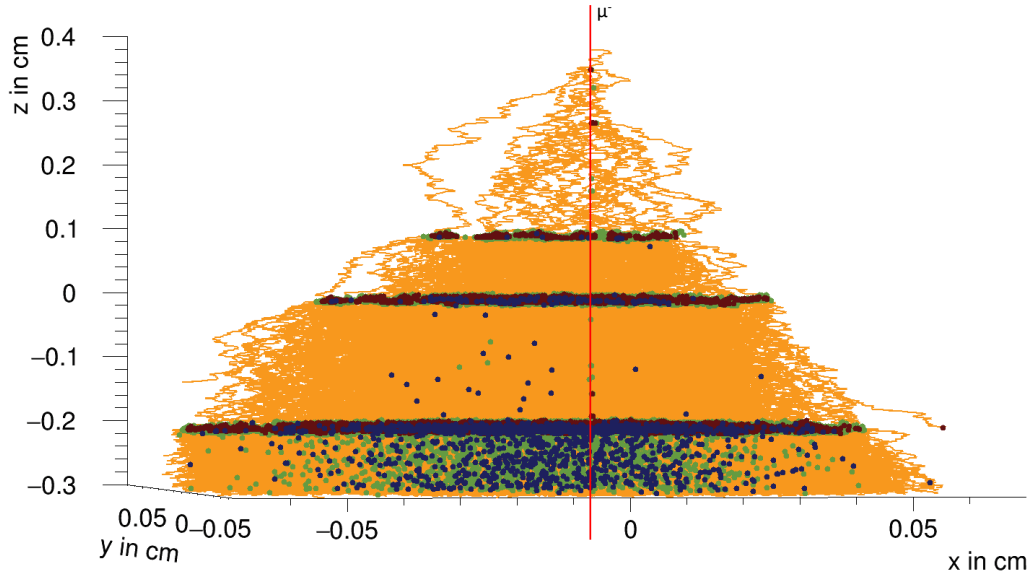

Figure 3.5: Full muon avalanche in a triple layer GEM stack setup. Muon path through the detector (red), drift lines (yellow), ionization (brown), excitement (green) and electron capture (blue) are shown. GEM foils located at z = 0.1 cm, z = 0.0 cm and z = -0.2 cm. Muon momentum is only in -z direction. Secondary ionizations can be seen along the muon path in the first drift gap as well as in the third drift gap.

3.2.3 X-ray photo-absorption simulation

`Heed` can also be used for the simulation of X-ray photo-absorption. This is implemented with the *TransportPhoton* class which uses basic parameters of the photon like initial position, energy and travelling direction and provides the number of electrons that were produced inside the detector volume.
One major drawback of this function is that it only provides the number of pho-

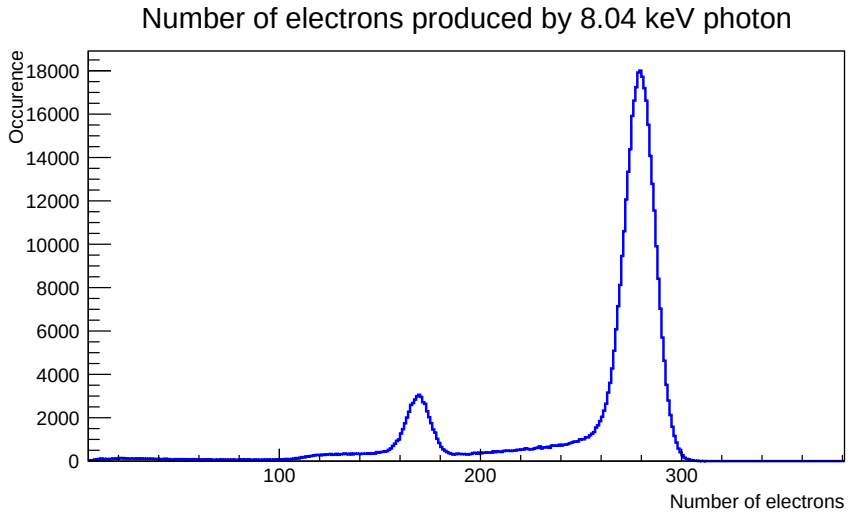

Figure 3.6: Number of electrons produced by a photon with the energy of 8.04 keV simulated in `Heed`. 5 Million photons were simulated, out of which only 9.3% produced any photoelectrons.

toelectrons produced in the process but neither the position of the electrons nor their energies.
Nevertheless, a brief simulation is done to look at the number of electrons produced by an incoming photon of 8.04 keV corresponding to the K_α peak energy of copper. In figure 3.6, the number of electrons produced by the incoming photon is shown. Two peaks are created; the second, larger peak is centered at 288 produced electrons. This is the number of electrons produced when the full photon energy is used to ionize the atoms. This can also be calculated by taking the average energy w required to produce one electron-ion pair in the gas.

$$N_p = \frac{8.04\,\text{keV}}{w_{\text{Ar}}} \cdot 0.7 + \frac{8.04\,\text{keV}}{w_{\text{CO}_2}} \cdot 0.3 \tag{3.1}$$

Equation 3.1 computes the number of produced electrons (N_p) for the 8.04 keV photon in an Ar/CO_2 70/30 gas mixture. w_{Ar} is 26 eV and w_{CO_2} is 33 eV according to [20].
This results in a theoretical number of 290 produced electrons. As seen in figure 3.6 this describes the second, larger peak.
The first, smaller peak is the escape peak of Ar that is due to the production of characteristic X-rays decreasing the apparent energy of the incident X-ray and yielding an offset peak.

Chapter 4

Analysis

4.1 Muon signal analysis

This first simulation aims at simulating muons passing through the detector to compute the previously defined primary electrons. In most cases however, only a single electron will be simulated. This is due to the opportunity of faster computation by parallel program executions.
Even when only a single electron is simulated, the objective is to very accurately simulate it as if it would have been produced by an ionizing muon. This way, the "same" electron can be simulated multiple times in order to obtain improved statistic significance.
Consequently, muons are first simulated without computing the consecutive electron avalanche. Applying this order allows for storing data for the primary electrons and then simulate electron avalanches according to their parameters.

4.1.1 Energy distribution of produced electrons

The most important parameter of this standalone muon simulation is the energy of the produced (primary) electrons. As described in chapter 3, this determines whether direct secondary ionizations can take place.
The simulation is done for muons with momenta of 1 GeV, 10 GeV, 100 GeV and 1 TeV.
This can be seen in figure 4.1. In the simulations the muon momentum is approximated as constant and thus the muons are not loosing energy while travelling through the detector (neither when ionizing a gas molecule nor when passing through the GEM foils).
The simulations do not show any meaningful differences for the different muon energies.

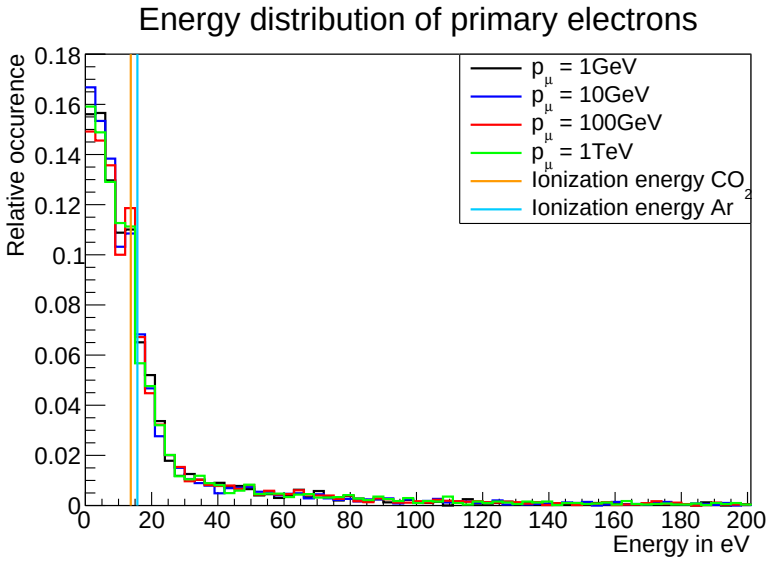

Figure 4.1: Energy distribution of primary electrons for muons with different momenta traversing through the chamber. Ionization energy of CO_2 at 13.78 eV and of Ar at 15.76 eV are also shown. Primary electrons above these energies may carry out immediate secondary ionizations.

Thus it was chosen to perform the following simulations with the single primary electrons' energy according to the distribution of the 1 GeV muon. This is achieved by assigning the starting electron a random energy according to the distribution of energies of electrons produced by the 1 GeV muons.

In figure 4.2, the number of primary and secondary electrons produced by each primary electron is shown. Obviously, the minimal number is one as the primary electron is always present. On average, each primary electron produces another 0.55 secondary electrons.

4.2 Single layer simulation

In this section, a detector consisting of only a drift plane, one single GEM foil and a readout plane is simulated and analyzed. This provides the advantage of generally reduced simulation times versus a triple GEM detector and thus the advantage of collection of more data points. Throughout this section, the induction gap ΔV_I is kept constant at 437 V and the drift gap ΔV_D is kept constant at 664 V which corresponds to the third GEM foil of the CMS GEM stack.

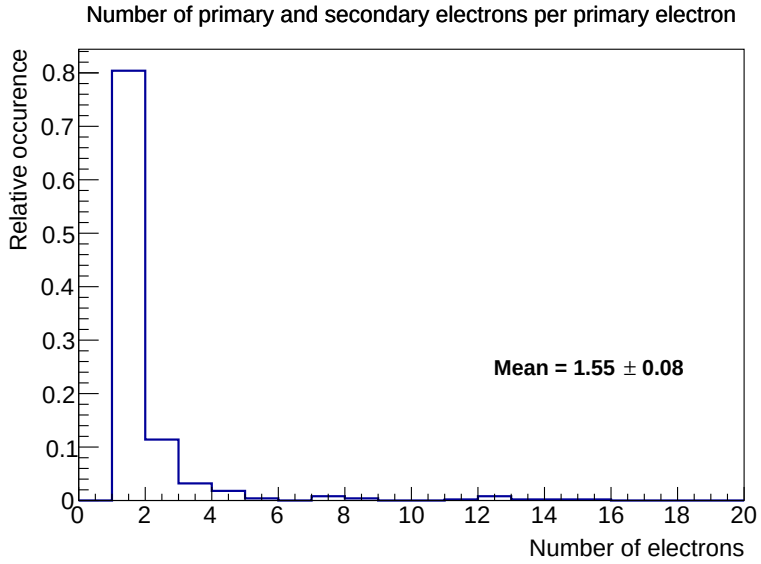

Figure 4.2: Number of primary and secondary electrons that are produced by a primary electron with a random starting energy chosen according to the 1 GeV muon from figure 4.1.

4.2.1 Voltage variation

As a first step, a single layer GEM is simulated at different potential differences between the top and bottom copper layers of the foil (ΔV) in the range between 360 V and 400 V. Knowing that at these voltages the gas detector gain is within the proportional region (see figure 2.4), an exponential relation is expected, shown in figure 4.3.

The primary transparency, as well as the foil transparency defined in chapter 2, is shown in figure 4.4; the transparencies are independent of the applied potential difference between the top and bottom of the foil. The primary transparency shows a small improvement for higher voltages and ranges from 85% to 93%. The foil transparency is constant at about 53%. Due to the independence of the applied potential difference, in further analyses the transparencies will just be looked at for a single ΔV.

It is important to note that the primary transparency describes the electrons which have produced any avalanche electrons at all. Primary electrons not producing an avalanche can either be due to electron capture above the first foil or termination on or in the foil prior to ionization of another atom. There are also cases for which avalanche electrons are produced, but they can not be “extracted” from the hole and all electrons terminate at the bottom of the foil. This is of course taken into account when computing the foil transparency.

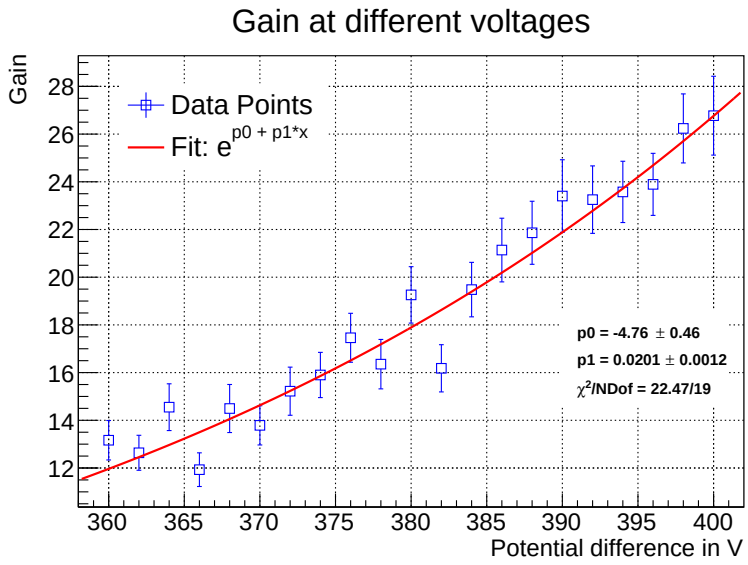

Figure 4.3: Gain as a function of ΔV with exponential fit. Nominal values for CMS GEM are (from top foil to bottom foil) $\Delta V = 394\,V$, $385\,V$, $368\,V$. Gain of one primary electron with starting energy according to the primary electron produced by a muon.

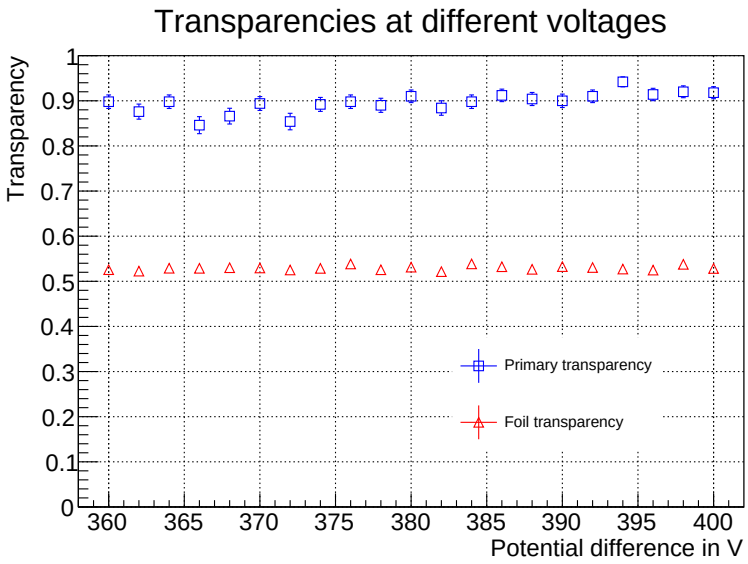

Figure 4.4: Primary transparency (blue) and foil transparency (red) for the single layer setup with different applied potential differences.

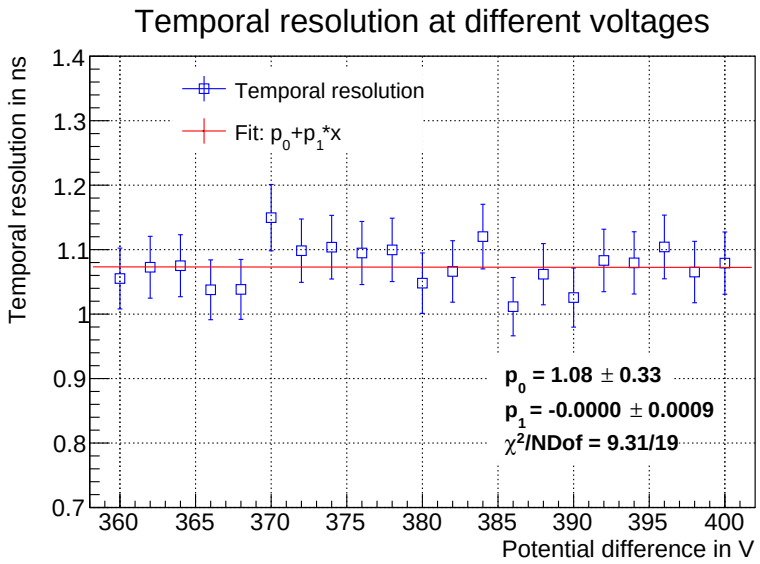

Figure 4.5: Temporal resolution on the readout plane of the single layer GEM for different ΔV. A linear fit with parameters is also shown.

For completeness, the temporal and spacial resolution are also considered in order to get reference points for further analysis.

The temporal resolution of the single layer simulation is shown in figure 4.5. A linear fit is done to the data points to study the dependence of temporal resolution to applied voltage. As can be seen from the slope of this fit, it is compatible with 0 and therefore it can be concluded that the temporal resolution of the single layer GEM does not depend on the applied voltage ΔV. For following simulations the temporal resolution will just be analyzed for a single ΔV, as well.

In figure 4.6, the spacial resolution is shown. The values shown for the spacial resolution in x and y direction are the standard deviations from a Gaussian fit to the distributions. A linear fit is performed on the resulting data in order to quantify the dependence of spacial resolution to applied voltage. As seen with the temporal resolution, the slopes of the fits are compatible with 0 and thus the spacial resolution is independent of the applied potential difference ΔV between the foils, the resolutions in the x and y direction are also compatible with each other as is expected due to the symmetry in the design. The signal is spread out about 130 µm to 140 µm on the readout plane.

In conclusion, the gain follows an expected exponential relation as a function of applied foil potential difference. The primary transparency and foil transparency, as well as the temporal and the spacial resolution, show no dependence on ΔV.

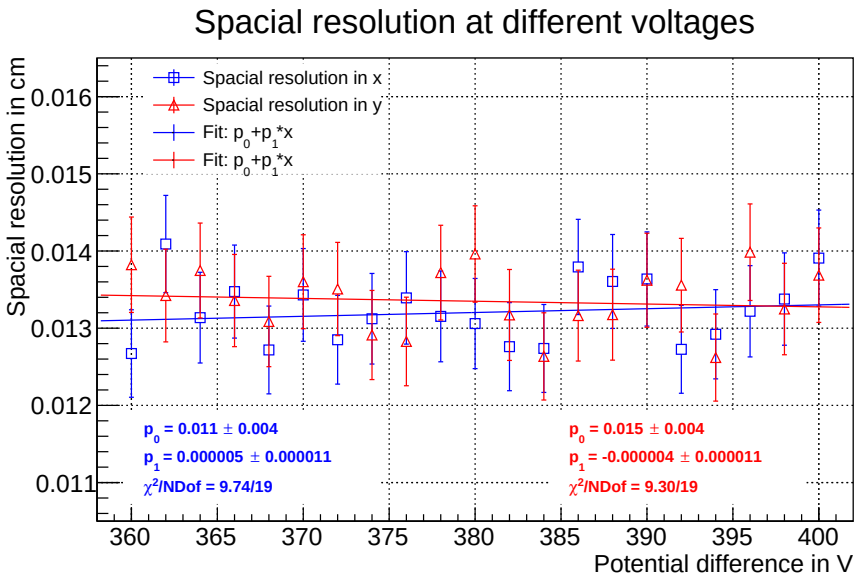

Figure 4.6: Spacial resolution on the readout plane in x direction (blue) and y direction (red) of the single layer GEM for different ΔV. Linear fits with parameters are also shown.

4.2.2 Gas mixture studies

In this part simulations for a single GEM foil are performed using different gas mixtures. This is a classical application of simulations, because testing new gas mixtures in real experiments could potentially damage the detector. When a suitable mixture is found, real experiments are needed to confirm its usability.

Table 4.1: Ionization potentials of gases used in the simulation. Taken from [12]

Gas	Ar	CO_2	O_2	N_2	H_2O
Ionization energy in eV	15.76	13.78	12.07	15.58	12.65

Varying the Ar/CO_2 ratio

The first simulations presented here consider various ratios of Ar/CO_2 inside the volume.
As mentioned, CO_2 acts as a quenching gas and also directly captures electrons of the avalanche. This is dependent on the electron energy at the point of impact with the CO_2 molecule. Resulting from the capture is the formation of an O^- ion

$$CO_2 + e^- \rightarrow CO + O^- \tag{4.1}$$

as presented in [13].

Table 4.2: Dissociative electron attachment peaks in CO_2 taken from [14]

Peak	Peak cross section
4.4 eV	1.43 $\times 10^{-19}$ cm^2
8.2 eV	4.48 $\times 10^{-19}$ cm^2

The simulations are carried out for Ar/CO_2 60/40, 65/35, 70/30, 75/25, 80/20 and 85/15.

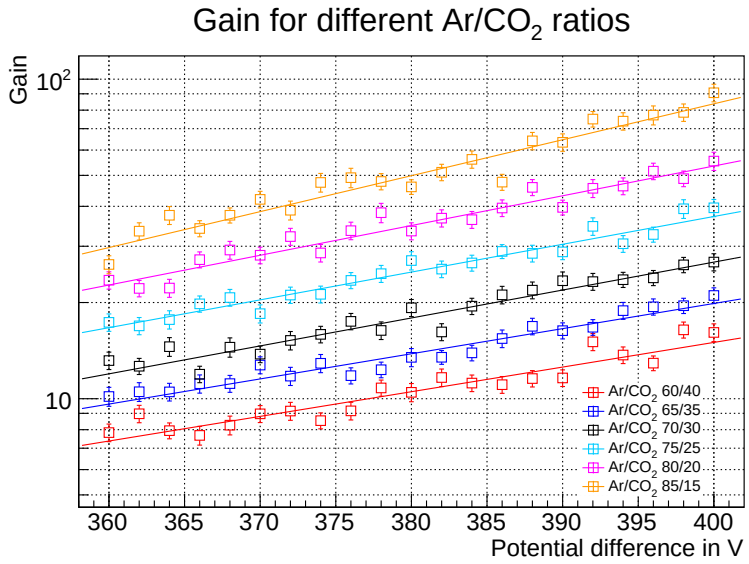

Figure 4.7: Gain as a function of ΔV with exponential fits for different gas mixtures of Ar and CO_2. CMS GEM nominal gas mixture is Ar/CO_2 70/30 (black).

In figure 4.7, the exponential relation of gain to applied foil voltage for different Ar/CO_2 ratios is confirmed. Furthermore, it can be seen that the relation of the gain to the argon fraction at a fixed voltage increases exponentially because less quenching gas is present (shown in Appendix A figure A.1). Still, an Ar/CO_2 ratio higher than 70/30 can not be used in the CMS GEM detectors because it would increase the probability of unintended discharges and thus damage the detector.
In figure 4.8, both transparencies are shown. The primary transparency does not depend on the Ar/CO_2 ratio, while the foil transparency decreases with increasing argon content above 70% with more electron endpoints on the bottom of the foil which might be due to less confinement due to reduced CO_2 fractions.

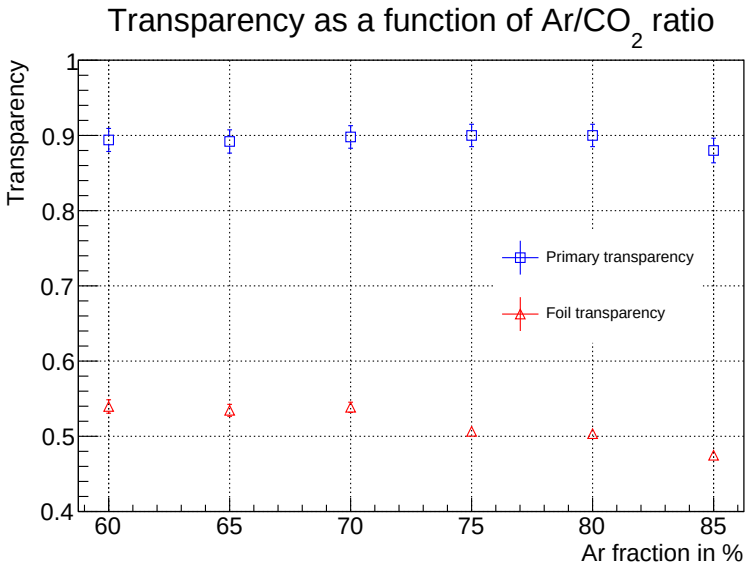

Figure 4.8: Transparency as a function of Ar/CO_2 mixture. Simulated for ΔV= 384V.

The time resolution shown in figure 4.9 worsens with rising argon content due to a slower drift velocity of the gas mixture. This effect is also described in [15]. The signal is also spread out more with increasing argon content because the CO_2 also acts as a cooling gas and confines the avalanche to a smaller area.

Leakage test: Adding air to the chamber

In this section, simulations with N_2, O_2 and an air mixture are carried out to predict the behavior of a leaking chamber.

The addition of small fractions of O_2 is expected to improve the gain due to the lower ionization potential of O_2 compared to the other gases in the mixture (compare table 4.1). However, when higher fractions of O_2 are added, the relative reduction in argon should reduce the gain.

O_2 also behaves similarly as CO_2, since electrons can be captured directly via dissociative electron attachment and the formation of an O^- ion

$$O_2 + e^- \rightarrow O + O^-. \tag{4.2}$$

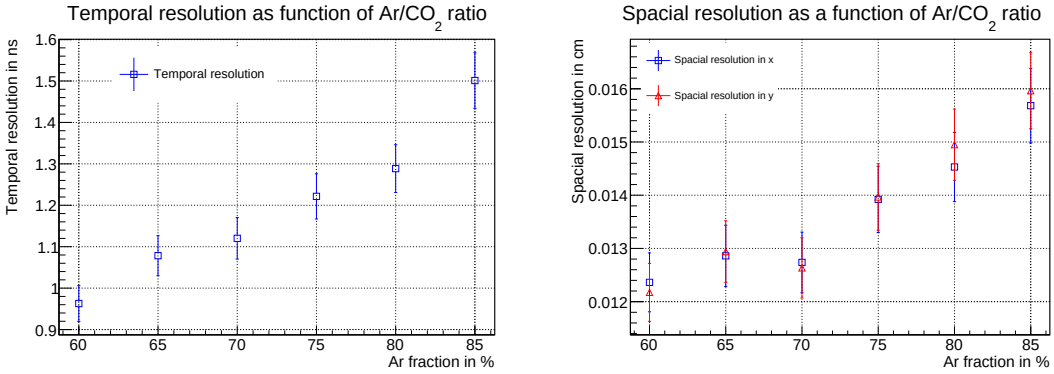

Figure 4.9: Temporal (left) and spacial (right) resolution as a function of Ar/CO_2 mixture. For the spacial resolution both the resolution in x and y directions are shown. Measured at $\Delta V = 384\,V$.

Table 4.3: Dissociative electron attachment peaks in O_2 taken from [13]

Peak	Peak Cross section
6.9 eV	13.4×10^{-19} cm^2

When comparing table 4.2 and table 4.3, the combined electron attachment cross section of O_2 is more than twice as big as the one of CO_2.
This shows that more electrons will be captured by O_2 than by only CO_2. This effect counteracts the effect of the higher gain because of the lower ionization potential.
In figure 4.10, the dependence of gain on the amount of added O_2 is shown. Only selected simulations for the addition of one, two and three parts are shown (all simulations are shown in Appendix A figure A.3) [1]. The addition of one part O_2 increases the gain, but larger fractions of O_2 decrease the gain again. This could be due to the relative reduction in argon or due to the dissociative electron attachment.
In figure 4.11, the transparencies are shown for an admixture of O_2. The primary transparency decreases at high admixtures of O_2. On further investigation, it becomes clear that this is due to primary and secondary electrons being captured before they can reach the foil. This also explains the loss in gain that can be seen in figure 4.10. This capture process outweighs the initial advantage of having

[1] The addition of one part does not mean the addition of 1%. The parts are normalized to 1 in the simulation and thus the percentages can be calculated. For example $Ar/CO_2/O_2$ 70/30/1 refers to a mixture of 69.31% Ar, 29.70% CO_2 and 0.99% O_2.

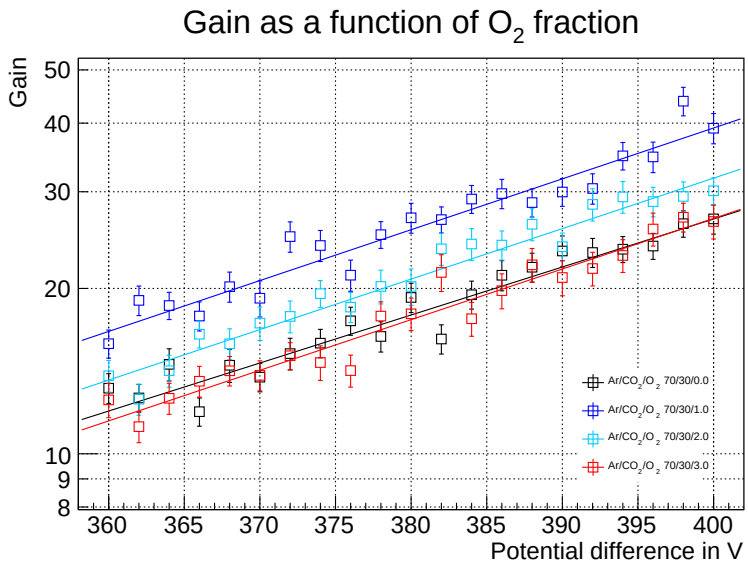

Figure 4.10: Gain as a function of ΔV for selected additions of O_2.

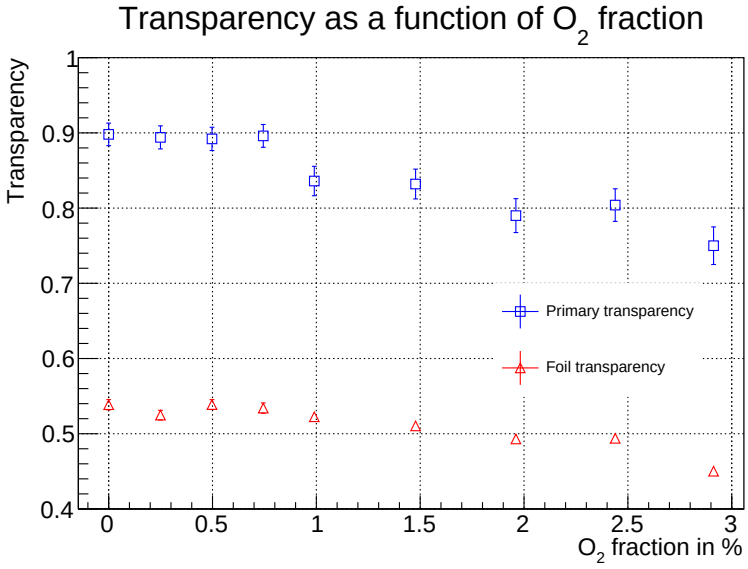

Figure 4.11: Transparency as a function of O_2 fraction. Simulated for ΔV= 384V.

a gas with a lower ionization potential in the mixture. This also affects the foil transparency because many of the electrons that are created in the foil are captured by the O_2 between the foil and readout plane.

In table 4.4, the percentages of electrons being terminated due to a dissociative electron attachment process and the number of total produced electrons are shown. It shows that a rising fraction of O_2 rapidly increases the probability for electron attachment to the gas. For large fractions the simulations were also done by replacing existing CO_2 by O_2 to keep the fraction of Ar constant. The total number of electrons produced rises initially for small fractions of O_2 due to the lower ionization potential, as discussed above, but decreases beneath the initial value due to the rise in electron attachment processes. For $Ar/CO_2/O_2$ 70/0/30 the 1.6 total produced electrons correspond to the number of primary and secondary electrons, thus no avalanche electrons are produced at all for this configuration.

Table 4.4: Fraction of electrons that are terminated due to a dissociative electron attachment process for different gas mixtures and average total number of electrons produced by a primary electron anywhere in the gas volume. Simulated at $\Delta V = 384\,V$

Gas mixture ($Ar/CO_2/O_2$)	Electron attachment	Total electrons
70/30/0	3.9%	36.2
70/30/1	6.9%	56.1
70/30/2	9.2%	49.3
70/30/3	11.6%	39.7
70/30/5	15.8%	32.7
70/30/10	28.5%	15.0
70/20/10	28.4%	24.1
70/0/30	100%	1.6

The temporal and spacial resolution show no change when varying the O_2 content (shown in Appendix A figure A.3).

Further simulations are done with an admixture of N_2. The gain is not expected to increase for small additions of N_2 as it was seen with the addition of O_2 because the ionization energy is not lower than the one of CO_2 (table 4.1).

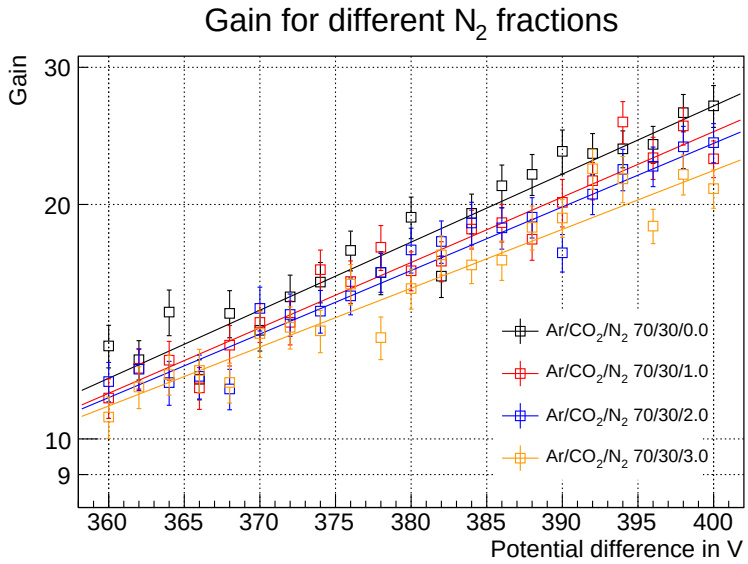

Figure 4.12: Gain as a function of ΔV with different selected additions of N_2.

As can be seen in figure 4.12, the gain does not change significantly with varying fractions of N_2. The small reduction that is observed can be attributed to the relative reduction of argon in the resulting gas mixture. Since the reduction of gain for the admixture of O_2 is higher than the one observed for N_2 it is proven that the reduction of the gain for O_2 is due to the increased dissociative electron capture rate.
In figure 4.13 no change in transparency can be observed.
In figure 4.14, the temporal and spacial resolutions with addition of N_2 are shown. While the spacial resolution is not impacted by the addition of N_2, the temporal resolution decreases (resulting in a sharper peak) for increasing N_2 content. This effect is also described in [15], where the impact of the addition of N_2 over the whole simulation range of electric field strengths present here is discussed.
The simulation with the admixture of both N_2 and O_2 in a ratio as in the air, concludes this section. A combination of effects of the previous simulations is expected.
With addition of air an initial increase in gain is not observed as was the case with addition of pure O_2. This is due to the fact that even for small additions of O_2 a rather high amount of N_2 needs to be added to achieve the correct gas mix for air. This results in relative reduction of argon in the mixture which reduces the gain further, outweighing the benefit of the lower ionization potential of O_2.
As seen in figure 4.16, the transparency does not change since the levels of O_2 at which an effect can be expected, are not reached here.
The temporal resolution for the addition of air (figure 4.17) shows the same trend

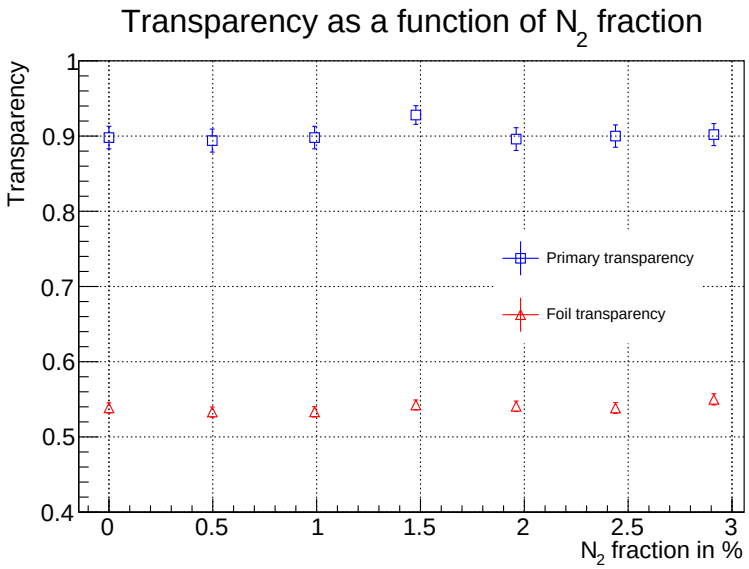

Figure 4.13: Transparency as a function of N_2 fraction. Simulated for ΔV= 384V.

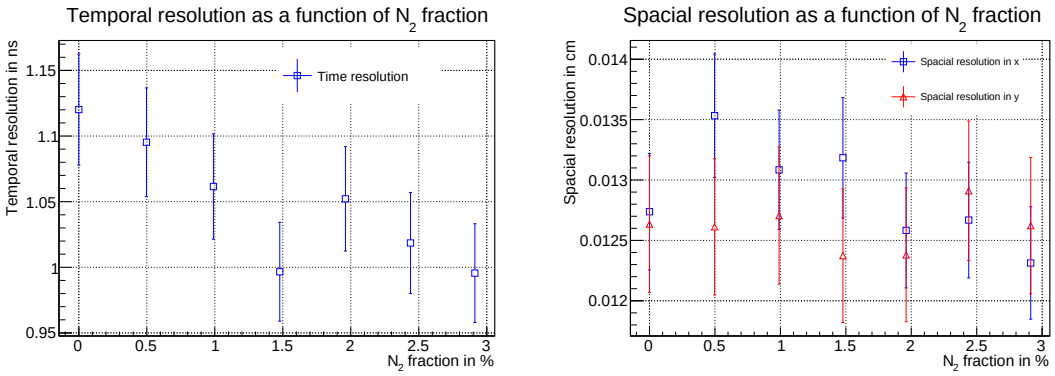

Figure 4.14: Temporal (left) and spacial (right) resolution as functions of N_2 fraction. For the spacial resolution both the resolution in x and y direction are shown. Simulated for $\Delta V = 384\,V$.

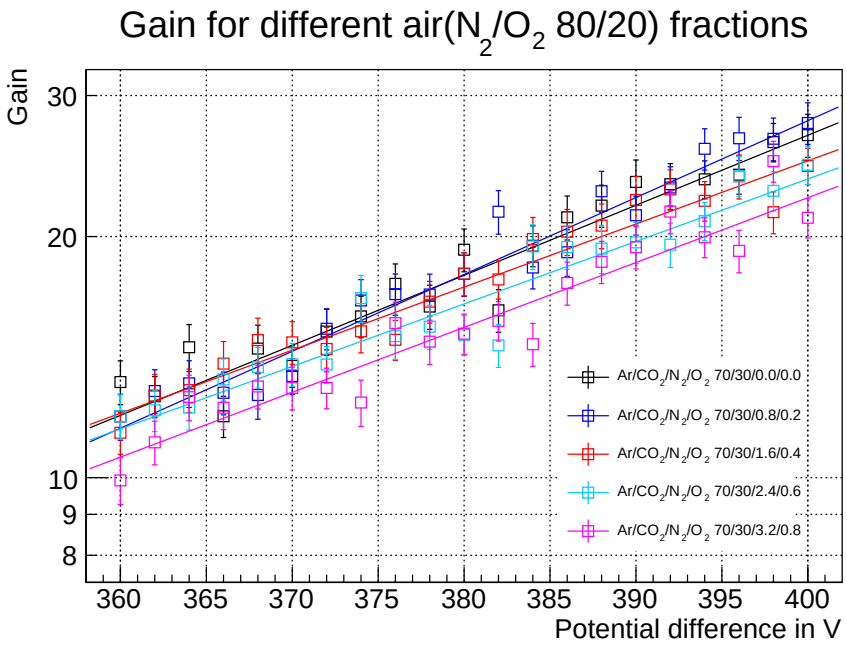

Figure 4.15: Gain as a function of ΔV with different additions of air.

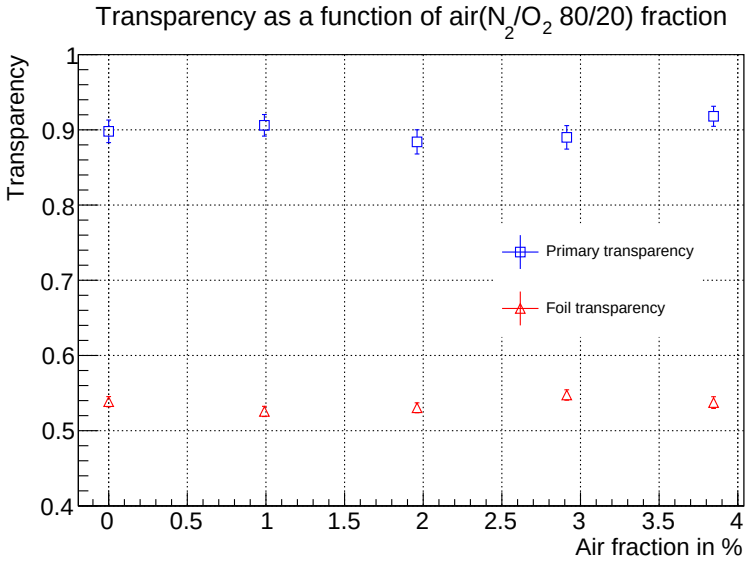

Figure 4.16: Primary transparency and foil transparency as a function of air fraction. Simulated for ΔV= 384V.

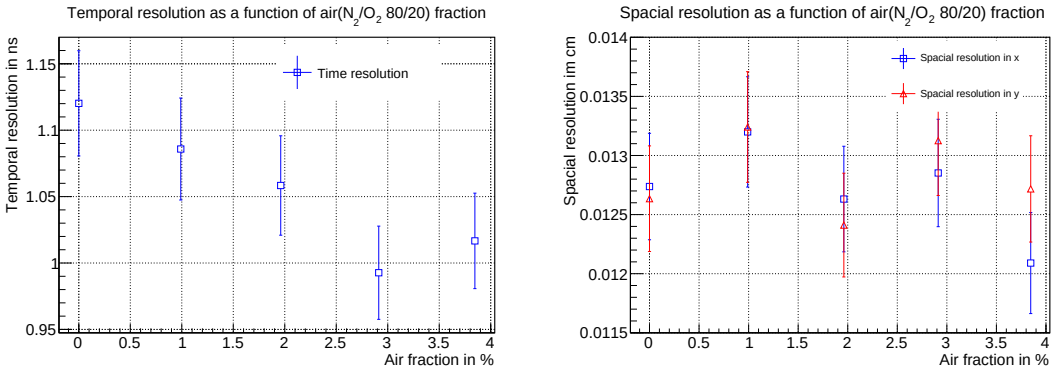

Figure 4.17: Temporal (left) and spacial (right) resolution as functions of air(N_2/O_2 80/20) fraction. For the spacial resolution the resolution in x and y directions are shown. Simulated for $\Delta V = 384\,V$.

as with the addition of pure N_2. This is consistent with [15] for the drift field strengths used.

Simulating humidity in the gas

One of the possible simulation gases of `Magboltz` is H_2O. It can be used to simulate humidity in the gas mixture.
To get an idea how much water needs to be added in order to achieve a realistic humidity in the gas mixture, the relative humidity is converted to the absolute humidity in the gas. Typical levels of relative humidity range from 40% to 70%.
A variation of the Magnus-Tetens formula to calculate the saturation vapor pressure as a function of temperature can be found in [11]:

$$P_{sat} = 6.112 \cdot e^{(17.67 \cdot T)/(T+243.5\mathrm{K})} \tag{4.3}$$

P_{sat} is the pressure at which the relative humidity is 100%, T is given in °C. Multiplying this equation by the relative humidity, the partial water pressure at a specific temperature for a given relative humidity can be calculated.
By approximating the gas to an ideal gas, the ideal gas equation $PV = nRT$ can be solved for $\frac{n}{V}$, which is the water amount in moles per volume.
The absolute humidity H_A in $\frac{\mathrm{mol}}{\mathrm{m}^3}$ can be calculated by

$$H_A = \frac{6.122 \cdot e^{(17.67 \cdot T)/(T+243.5\mathrm{K})}}{(273.15\mathrm{K} + T) \cdot 0.08314} \cdot H_R \tag{4.4}$$

with H_R being the relative humidity ranging from 0 to 1.
Since one mol of gas at 20°C and a pressure of 1013 hPa occupies a volume of 24 L, the fraction of water vapor in the gas mixture can be computed.

Table 4.5: Converting relative humidity to absolute humidity using equation 4.4

T	Rel. humidity	Absolute humidity	Fraction of H_2O in gas volume
20°C	25%	0.24 $\frac{\text{mol}}{\text{m}^3}$	0.58%
20°C	50%	0.48 $\frac{\text{mol}}{\text{m}^3}$	1.15%
20°C	75%	0.72 $\frac{\text{mol}}{\text{m}^3}$	1.73%
20°C	100%	0.96 $\frac{\text{mol}}{\text{m}^3}$	2.30%

To achieve a good understanding of the effect humidity has on the signals of the chamber, additional simulations are done at approximately these fractions of H_2O. As is the case for O_2, H_2O has a smaller ionization potential than the other gases in the mixture (see table 4.1).

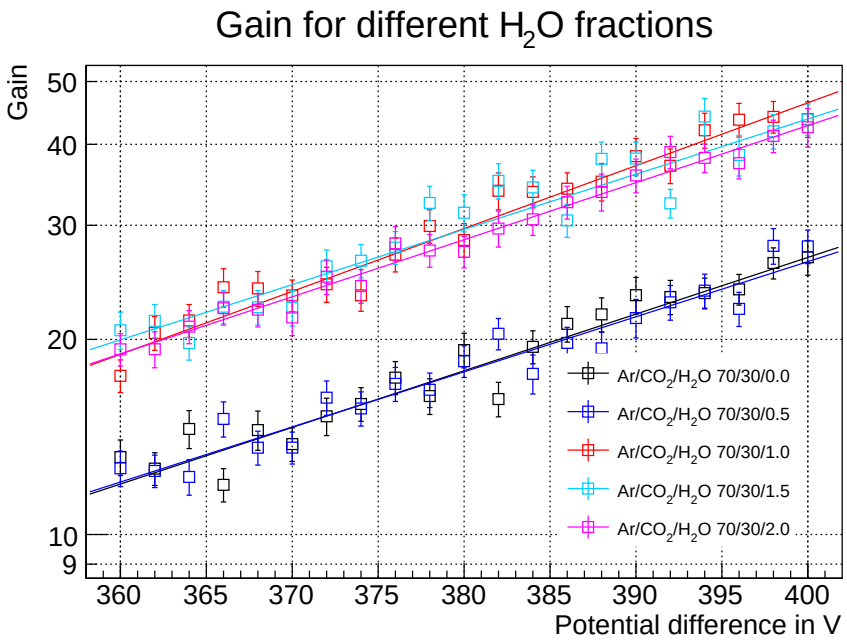

Figure 4.18: Single GEM Gain as a function of ΔV for different admixtures of H_2O simulating humidity in the chamber.

As can be seen in figure 4.18, the addition of H_2O increases the gain as expected due to the lower ionization potential. Remarkably, the gains for 0 and 0.5 parts H_2O addition and the points for 1.0, 1.5 and 2.0 parts H_2O addition overlap. There is no physical explanation for this, but it might be due to some approximations done in the simulation. As described in [21], H_2O is not simulated by `Magboltz`

with the same accuracy as the other gases used and this might be the reason for the observed "clustering" of gain curves.
A gain reduction for higher admixtures of H_2O did not occur due to the relative reduction in argon, further studies with even higher contents of added H_2O could be made to investigate this. This however would represent a relative humidity of more than 100% at normal conditions, which is unphysical.
The transparency, the temporal and the spacial resolutions stay constant under these conditions (Appendix A figure A.4).

4.2.3 Geometry studies

As mentioned in chapters 1 and 2, GEM detectors can have very different geometries.
GEM foils are produced by etching copper and Kapton with different acids. The production and assembly takes place inside a clean room to prevent short-circuits of the foils by dust particles. Because the production utilizes acid and the GEM geometrical structure is small (nominal 140 µm pitch, 70 µm outer diameter and 60 µm foil thickness), not all holes are identical. In this section it is studied how deviations from the nominal geometrical values, outlined in [1], effect the performance of the GEM detector.

Hole pitch

When varying the hole pitch, the hole/surface ratio of the GEM foils changes as well. The electric field strength inside the holes stays the same.
In figure 4.19, the gain for varying hole pitches is shown. It does not show a clear trend and seems rather constant apart from the 110 µm point. A higher value can be observed at 140 µm, which is the nominal value of the CMS GEM foils. However, this "peak" could also (partly) be due to statistical fluctuations and more simulations are needed to prove the significance of this result.
In figure 4.20, the primary and the foil transparencies are shown. The expected drop in primary transparency due to a lower hole/surface ratio at larger hole pitch is seen. For smaller hole pitch, the primary transparency does not increase above 95%. This indicates that up to 140 µm the electric field guides the electrons to the holes and only for larger pitches not all electrons can be guided into the holes.
It is remarkable that the foil transparency increases for higher hole pitch. This might be due to a better extraction of electrons out of the holes due to the distorted electric field from the holes interfering less with the fields of neighboring holes. A plateau starting from around 140 µm can be seen. This seems to be a point where the influence of the neighboring holes becomes less significant.

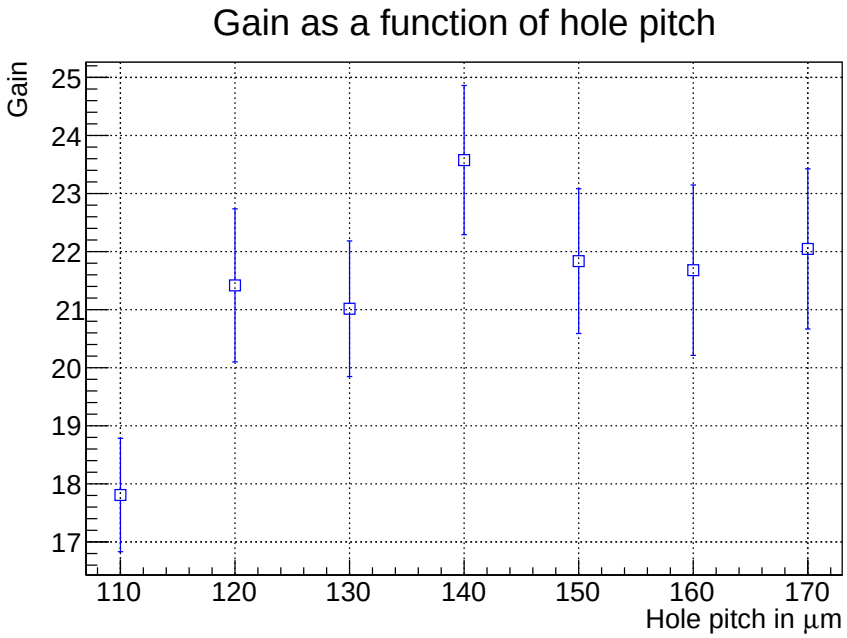

Figure 4.19: Gain as a function of GEM hole pitch in the range from 110 µm to 170 µm. Measured at ΔV= 394V.

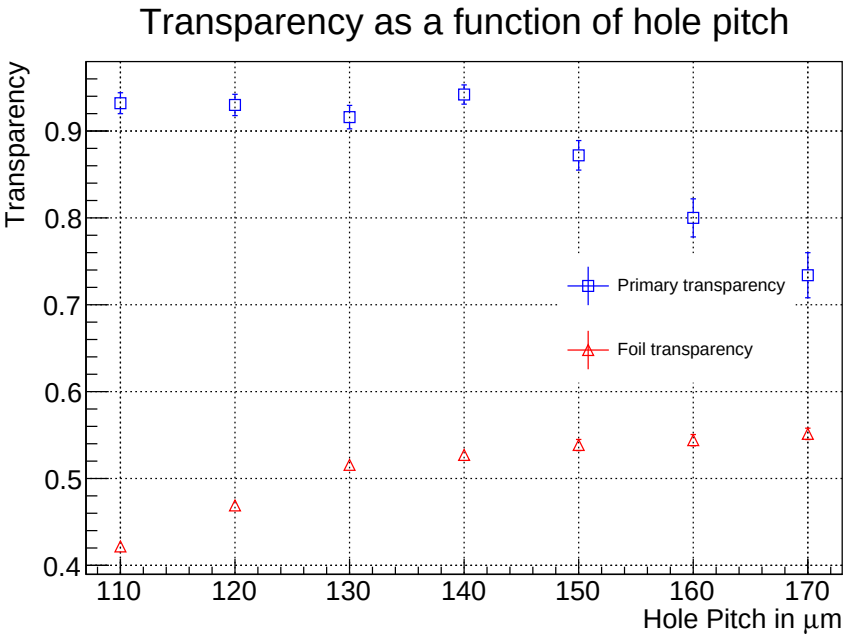

Figure 4.20: Transparency as a function of hole pitch in the range from 110 µm to 170 µm. Measured at ΔV= 394V.

Overall, when looking at the gain again, it seems that the effects of primary and foil transparency almost cancel out each other. The peak at 140 µm is the point where the primary transparency is still on its plateau, and the foil transparency has just reached its plateau which could explain this small peak in the gain data. The temporal and spacial resolutions do not show a dependence on the hole pitch (Apppendix A figure A.6).

Hole diameter

The diameter of the holes is also varied with a starting point of 70 µm for the outer diameter and 50 µm for the inner diameter. The inner diameter is set to be 20 µm smaller than the outer diameter for all settings.
Increasing the hole diameter decreases the electric field strength in the middle of the hole because it is a further distance away from the copper plates, as shown in table 4.6.

Table 4.6: Electric field strengths at the edge and in the center of the hole for different hole diameters at a ΔV of 394 V and a hole pitch of 140 µm. Both are measured in the middle of the hole where the diameter of the hole is the smallest.

Diameter in μm	Edge E-Field in kV/cm	Center E-Field in kV/cm	Ratio
55	61.3	54.2	0.88
60	61.9	52.6	0.84
65	62.2	50.6	0.81
70	62.3	48.9	0.79
75	61.6	47.8	0.78
80	61.1	46.8	0.77
85	61.0	44.3	0.76

In figure 4.21, the gain as a function of diameter is shown for a single potential difference. The gain peaks for 70 µm at a hole pitch of 140 µm. This is the diameter of the CMS GEM default setup. For higher diameters the gain worsens and reaches about 2/3 of the peak gain for an outer hole diameter of 85 µm.
Looking at the transparency in figure 4.22 it can be seen that the primary transparency increases from 70% for a diameter of 55 µm to a constant 90% primary transparency for diameters over 70 µm. The primary transparency increases because the hole-to-foil-ratio changes. It saturates because from some point onwards

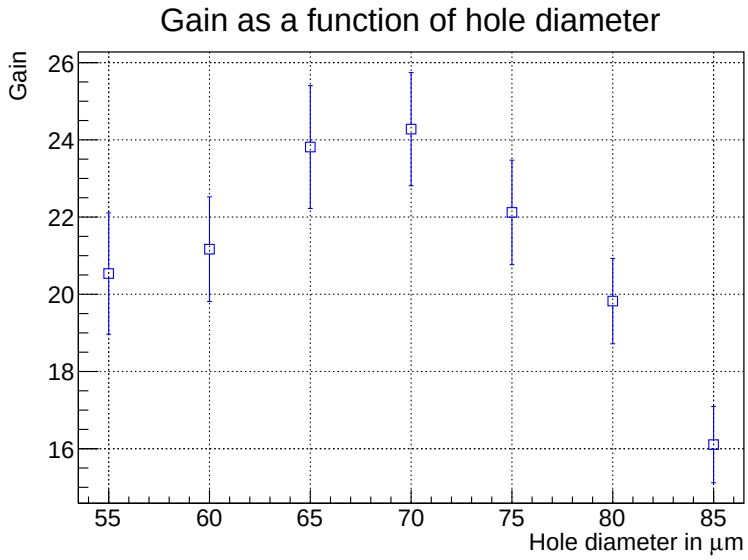

Figure 4.21: Gain as a function of GEM hole outer diameter in the range from 55 µm to 85 µm. Simulated for ΔV= 394V.

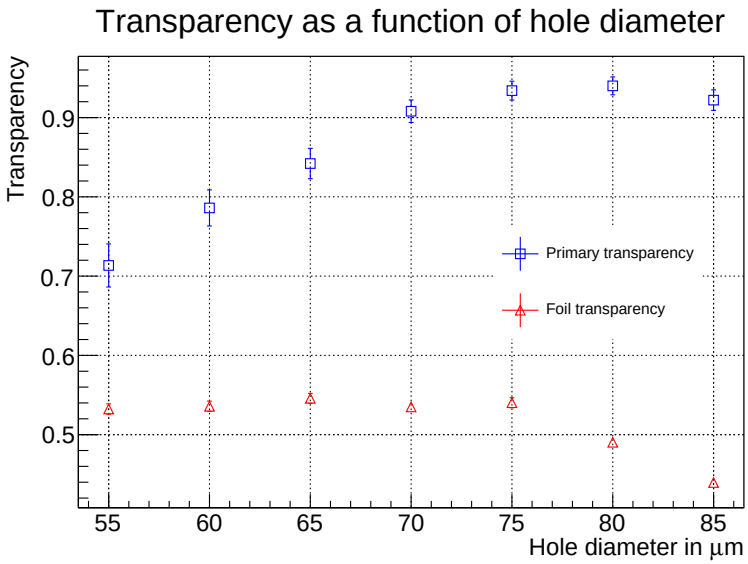

Figure 4.22: Transparency as a function of GEM hole outer diameter in the range from 55 µm to 85 µm. Measured at ΔV= 394V.

the electrons can be guided into the holes reliably, as was already discussed for the hole pitch. This initially lower primary transparency explains the lower gain shown in figure 4.21 and is due to more electrons hitting the top of the GEM foil. The foil transparency is stable for small diameters and decreases starting from 75 µm. This could again be due to the influence of neighboring hole fields to the electrons exiting the hole region. This in turn explains the rapid drop in gain for higher diameters as the foil transparency has a big impact on the gain.
The spacial and temporal resolutions stay constant throughout the variation (Appendix A figure A.5).

Foil thickness

In the next simulation the foil thickness is varied. The starting point for this simulation is the nominal value of 60 µm thickness, with a Kapton layer of 50 µm in the middle and 5 µm of copper on either side of the foil. It should be noted that the 5 µm of copper are kept constant and only the Kapton thickness is varied.
When increasing the foil's thickness, the electric field strength decreases at the same applied potentials. This leads to a reduced gain for increasing foil thickness. The expected relation of higher foil thickness to lower gain is observed in figure 4.23. From this simulation alone, it might seem that a thinner foil might produce better results for the real chamber, but it has to be noted that the probability of discharges increases with higher electric field strengths. This is not simulated

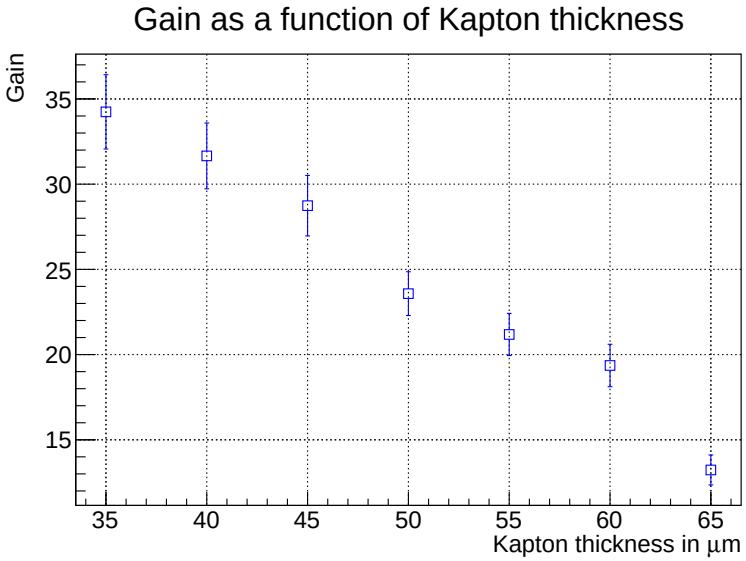

Figure 4.23: Gain as a function of Kapton thickness in the range from 35 µm to 65 µm. Measured at $\Delta V = 394V$.

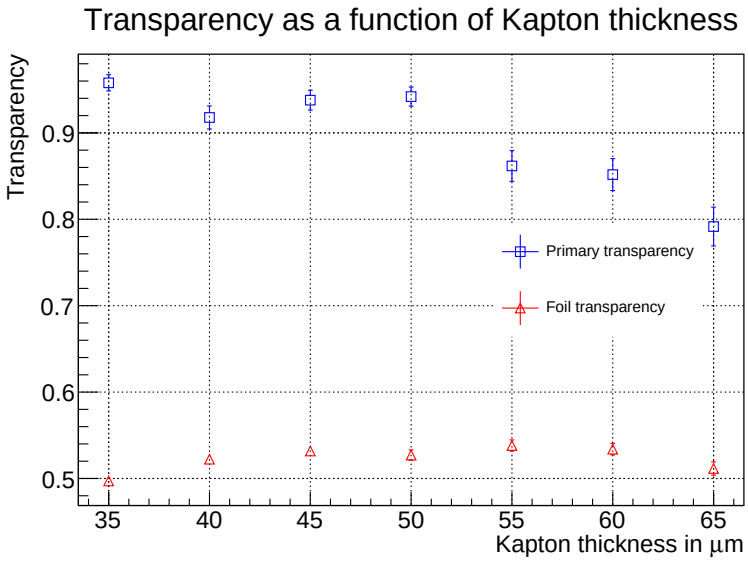

Figure 4.24: Transparency as a function of Kapton thickness in the range from 35 µm to 65 µm. Simulated for ΔV= 394V.

here.
The transparency also changes with respect to the Kapton thickness, as shown in figure 4.24. While being constant for a Kapton thickness of up to 50 µm, for higher Kapton thicknesses a drop in primary transparency is observed. This is also due to the reduced field strength as the electrons do not get pulled into the hole as much as with the default setup and therefore more electrons hit the top of the foils. The foil transparency stays roughly constant for a variation of Kapton thickness.
The temporal and spacial resolutions show no dependence on Kapton thickness (Appendix A figure A.7).

Straight Hole shape

As shown in figure 3.1, the holes have a double-conical cutout. A detector setup with a straight cylindrical hole can also be imagined.
The gain of such a detector would be expected to increase because there are no protruding Kapton edges for the electrons to hit in this case.
The simulation of such a foil is done in the single layer setup, and it is compared to the CMS GEM standard setup.
As can be seen in figure 4.25, the gain increases by a factor of approximately 1.5. Even though this design increases the gain, the conical cutout design is generally used because it reduces the chance for discharges between the top and bottom copper layer. The simulation presented here does neither simulate discharges nor

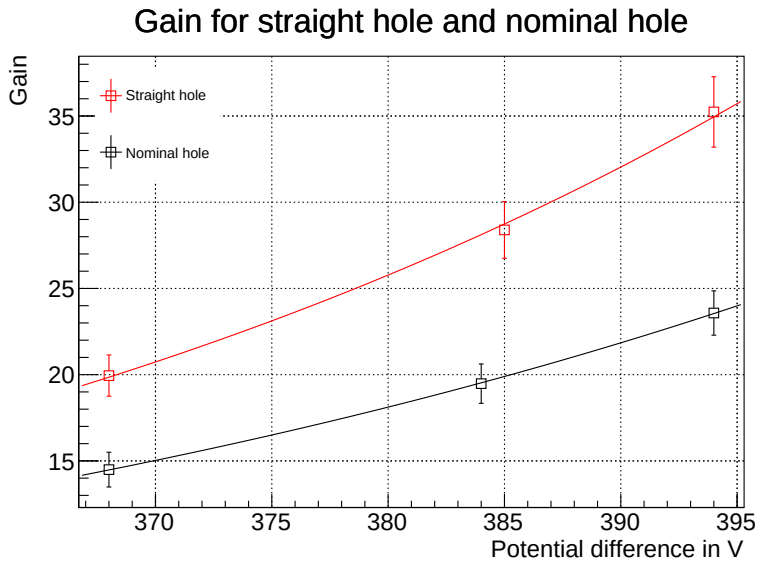

Figure 4.25: Gain for straight and nominal CMS GEM hole as a function of ΔV.

compute discharge probabilities.
When using a straight hole the gain could be kept constant by reducing the applied voltage and thus the electric field inside the hole to prevent a higher discharge probability.
Furthermore, in reality the protruding edges of the Kapton inside the hole accumulate electrons over time which might help to guide the electrons through the waist of the hole [27]. This however is not simulated here as electrons are terminated once they hit a geometrical feature and leave no charge behind to influence future electrons.

Single mask GEM

Up to here, foils produced using the double mask process were simulated. The starting point for these simulations were the specifications outlined in [1].
Recently, a single mask GEM production process has been established for the CMS GEM detectors. This results in a different hole geometry. Instead of having a symmetric hole structure with outer diameters of 70 µm on both sides, the bottom side now has a diameter of 85 µm. The inner diameter of 50 µm stays constant. A sketch is shown in figure 4.26.
When looking at the real GEM foil (figure 4.27) the rim (the 5 µm copper cutout in front of the conical hole shown in figure 2.1) can not really be made out, in fact, sometimes it looks as if an inverse rim is present. Since this last variation of geometry is intended to represent the reality as precisely as possible, both

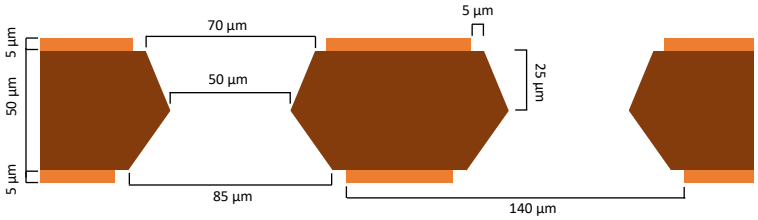

Figure 4.26: Sketch of a GEM foil produced with the single mask configuration as outlined in [17].

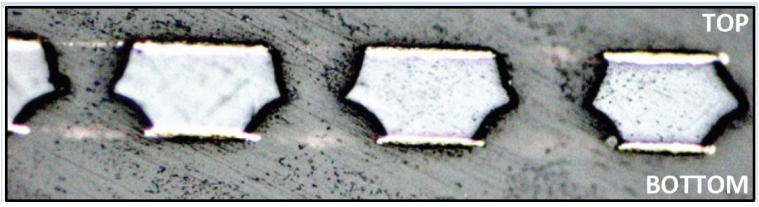

Figure 4.27: Picture of a GEM foil produced with the single mask process (from [17]). Shown is the "bottom" orientation (meaning the larger diameter is on the bottom of the foil and thus located in direction of the readout plane), the middle diameter of 50 µm is located in the vertical center of the foil.

orientations of the single mask GEM, as well as the double mask foil, are simulated with and without a rim in this section.
In figure 4.28, the gain of the six possible different configurations is shown. The gain for the configurations without a rim is always higher than in the same configurations with a rim. This is expected, because including a rim decreases the electric field strength. The double mask GEM has a higher gain than the single mask GEMs in both orientations. This is also due to the electric field strength decreasing inside the hole for the single mask GEMs.
In figure 4.29, the primary and the foil transparencies of the six possible configurations are shown. Omitting the rim causes the primary transparency to drop; more electrons are hitting the top of the foils and are not guided into the holes as reliably as in the other configurations. The configuration for the lowest primary transparency both with and without a rim is the single mask bottom configuration. The double mask geometry lead to a slightly higher transparency, having the same diameter at the top opening as the single mask bottom configuration. Since the electric field strength is greater for the double mask setup, the electrons are guided better than with the single mask bottom setup.
The foil transparency also deserves attention. It is smallest for both the double mask without rim and the single mask "top" orientation without rim. With these geometries more electrons stick to the bottom of the foils. All other geometries

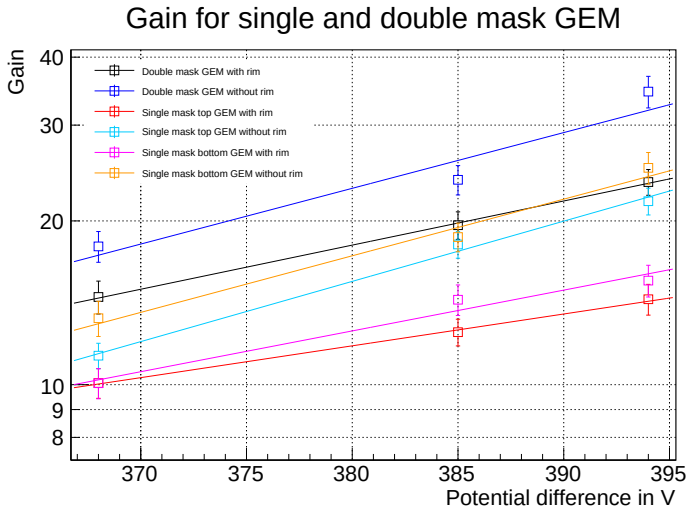

Figure 4.28: Gain for a single layer GEM with different hole geometries. Double mask with (black) and without (blue) rim shown as simulated above. Single mask GEM with larger diameter on the top with (red) and without (azure) rim as well as single mask GEM with the larger diameter on the bottom with (magenta) and without (orange) rim are also shown.

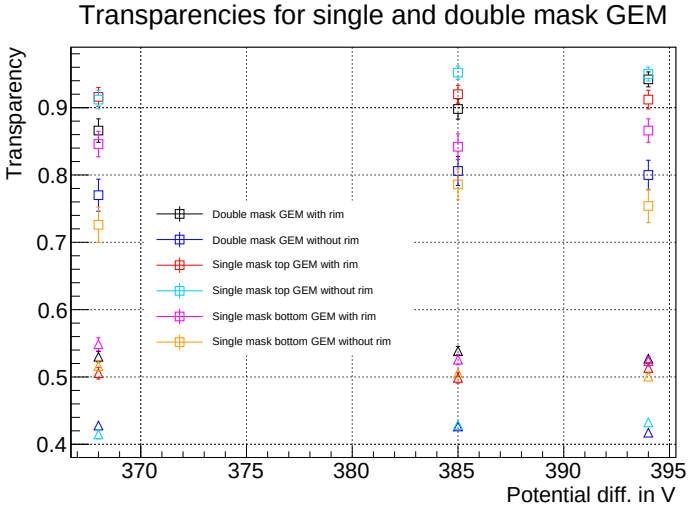

Figure 4.29: Primary (square) and foil (triangle) transparencies for a single layer GEM with different hole geometries. Double mask with (black) and without (blue) rim shown as simulated above. Single mask GEM with the larger diameter on the top with (red) and without (azure) rim as well as single mask GEM with the larger diameter on the bottom with (magenta) and without (orange) rim are also shown.

show the same foil transparency. With a larger opening at the bottom or with a rim, the foil transparency saturates at about 53%-55%.

4.2.4 Shorted foil

Each CMS GEM detector foil is segmented into 47 (long-chamber) or 40 (short-chamber) high voltage sectors. If a short-circuit occurs in one of the sectors, it is shut off by a protection resistor of 10 MΩ. The remaining 46 (39) sectors of the foil remain fully functional but are now at a different (lower) potential difference due to the additional 10 MΩ resistance in parallel.

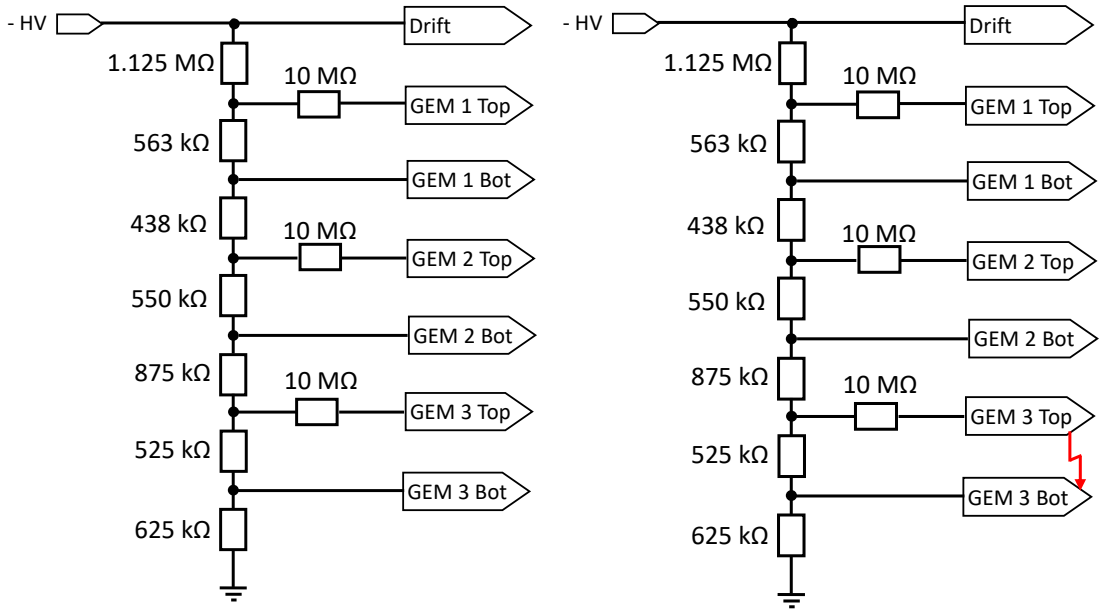

Figure 4.30: GE1/1 high voltage divider without short circuit in normal operation (left) and with short circuit in GEM 3 (right). The protection resistors with 10 MΩ are located on the GEM foils, one for each of the 47 GEM foil sectors.

In the experiment, the current is kept constant at a working point of 650 µA. If a short circuit in one sector of one foil occurs, only the potential difference between the top and bottom of this foil is changed while all other gaps and foils stay at a constant potential difference due to the constant current operation of the GEM detector.
In figure 4.30, the high voltage divider used in CMS is shown.
If a multi channel HV supply is used, each of the seven electrodes can be supplied with an individual voltage. If a short circuit occurs in one (or more) sectors of a

foil this can be corrected by the multi channel HV supply as long as the power supply can provide the current through the protection resistor ($\sim \frac{400\,\mathrm{V}}{10\,\mathrm{M\Omega}} = 40\,\mu\mathrm{A}$). Because the normal resistor between the sectors is 563 kΩ, 550 kΩ and 525 kΩ, respectively, and the protection resistors are 10 MΩ per foil, the new potential difference over the still working part of the foil should be about 95% of the potential difference without a short circuit. This varies slightly depending on the foil the short circuit occurs in.
This has the same effect as reducing the voltage difference of the foil, which was already simulated in chapter 4.2.1.
Of course the sector where the short circuit occurs will be at a potential difference of 0 V.

Complete foil failure

To understand the electrons' path through a foil segment with a short circuit, a simulation with a potential difference of 0 V over the whole simulation area is carried out. The parameter of interest here is the fraction of electrons that traverse the foil into the next drift gap.

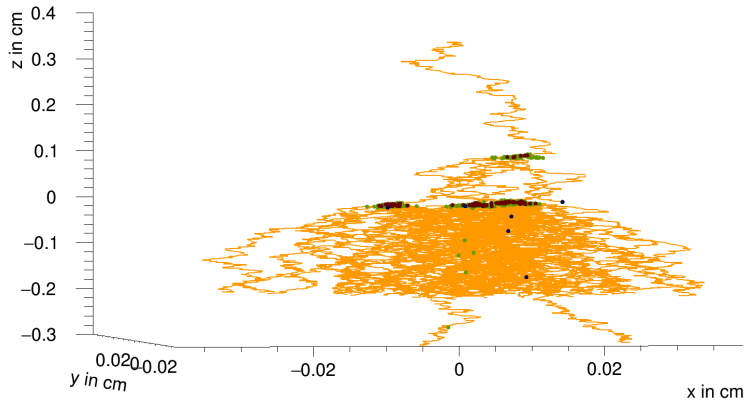

Figure 4.31: Avalanche of a sample electron with a shorted GEM 3 foil. The electron avalanche takes place in the first GEM layer at z = 0.1 cm and the second GEM layer at z = 0 cm, but most of the avalanche electrons terminate at z = −0.2 cm, where the third, shorted GEM foil is located.

In figure 4.31, an example avalanche for a failed GEM 3 foil with a ΔV of 0 V is shown. The simulation of 10000 primary electrons shows that 2.6% of these electrons pass the foil. To compare this with the geometric fraction of holes to the foil this ratio is calculated. This is done at the smallest diameter of the hole, 50 µm. This leads to a hole/foil ratio of 11.6%. The number of electrons that can

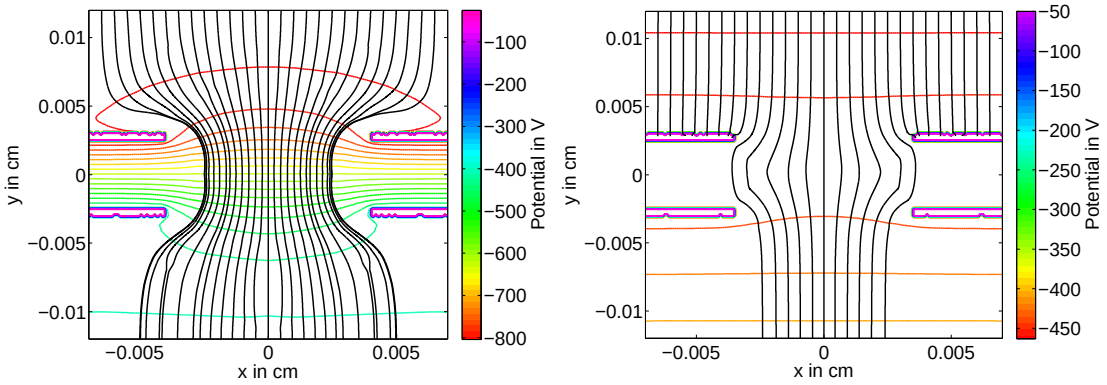

Figure 4.32: Equipotential lines (color coded) and stream lines (black) for a working setup with $\Delta V = 384\,V$ (left) and the short-circuit setup (right). The stream lines were plotted using the `MATLAB` function *streamline*. The streamlines simulate the idealized path a massless particle travelling in a vacuum would take.

pass through the hole is much smaller than the number that could pass through it following the geometrical constraint.
This is due to the top copper layer now acting as an anode for the electrons. They are no longer guided inside the holes but are now guided onto the top of the foil. This means that this foil segment can be considered nearly dead and allows almost no electrons to pass.
This can also be seen in figure 4.32 where the potential field of one hole for the default and the shorted foil are shown. Note that for the shorted foil the electrons are now guided onto the top copper layer and the few that make it into the hole are guided further onto the protruding edge of the Kapton (not shown in figure 4.32).
Since avalanches are normally not spread out over multiple HV sectors of the foil, entire avalanches can effectively be "stopped" by a short-circuit but avalanches in the other 46 (39) functioning sectors are only slightly effected due to the lower ΔV and can still be detected. If an entire foil were to fail (it is highly unlikely that multiple short circuits would cause this) in the triple GEM detector, no signals could be read out by the readout board anymore.

4.3 Triple layer simulation

To better understand the whole GEM setup used in the CMS GEM detectors, the complete stack is simulated in this section.
First, the detector with default parameters is simulated.
In figure 4.33, the gain at the different layers of the GEM stack is shown.

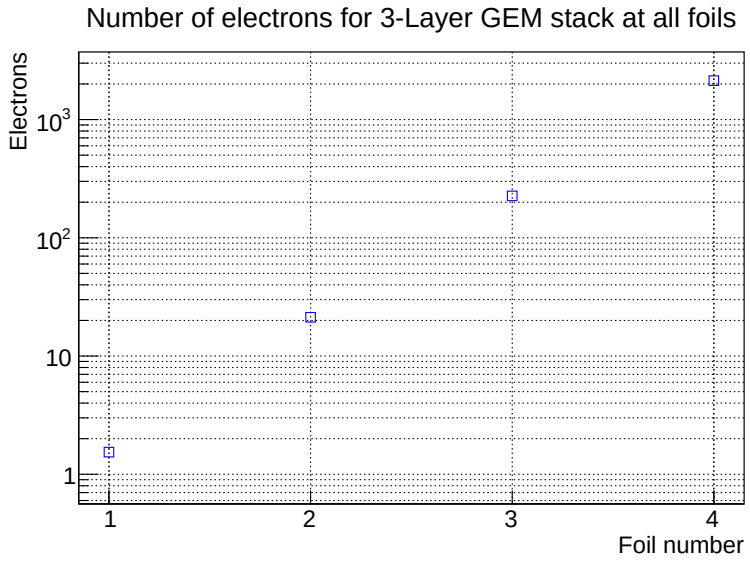

Figure 4.33: Gain at different locations of the triple GEM stack with standard parameters. On the x axis the foil number is shown; the point at $x = 4$ refers to the gain at the readout plane.

The final gain is 2130 ± 140 at the readout plane. To check if this is in accordance with the single layer simulation, the theoretical triple layer gain is calculated from the simulated single layer gain. For this, the fit shown in figure 4.3 is used. For every single layer GEM simulation a primary electron that could produce secondary electrons was simulated and in the triple layer simulation only one primary electron that could produce secondary electron was placed above the GEM stack. Due to this, the results obtained in the single layer simulation need to be normalized by the average number (1.55 ± 0.08 as can be seen in figure 4.2) of produced secondary electrons to be able to compare the results to the triple layer simulations.

The expected triple layer gain is 2420 ± 250, which is within one σ of the simulated triple layer gain.

A histogram of the times at which the electrons hit the readout plane is shown in figure 4.34. It shows a time resolution of 1.76 ± 0.09 ns for a single starting primary electron. As it is only measured over which time span the electrons hit, this can not be related to the real GEM chambers as readout electronics are not taken into account here and as this is only the simulation for a single primary electron. The absolute time (91.9 ns) can be expected to be similar in experiments as this mostly represents the drift velocity of the electrons. The spacial distribution is also shown in figure 4.34.

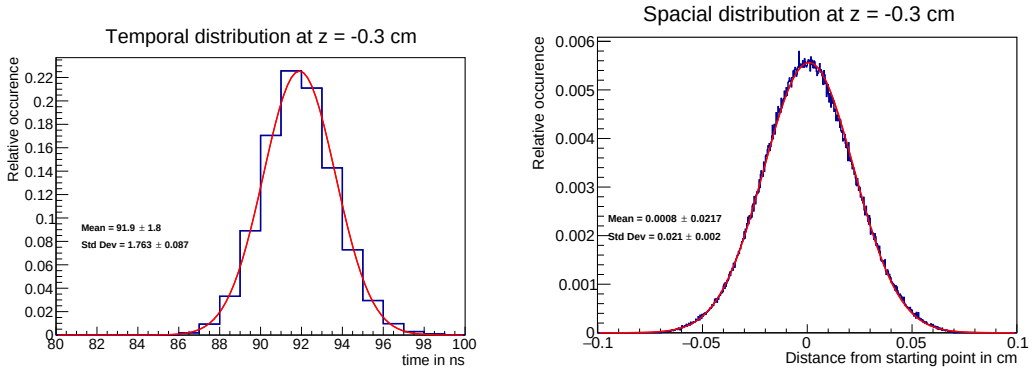

(a) Temporal distribution

(b) Spacial distribution

Figure 4.34: Temporal and spacial distribution at the readout board for the triple layer default setup CMS GEM stack. Resolution obtained from the Gaussian fits.

4.3.1 Environmental influences

Since GEM detectors are gaseous devices, the influence of the ambient environment has to be considered. For accurate measurements, the signals of the GEM detectors need to be corrected for these parameters.

Pressure

The pressure of the gas inside the detector is roughly equal to the pressure of the surrounding environment (a small overpressure of a few hPa is created in operation due to the continuous gas flow).
This parameter is extremely relevant for the quality control (QC) measurements. Because they are performed in different sites in countries spread across the world with different elevations above sea level, the ambient pressure can vary significantly.
When varying the pressure, the mean free path of an electron in the gas mixture is changed. The mean free path can be estimated by the formula

$$\lambda = \frac{1}{n \cdot \sigma} \tag{4.5}$$

where σ is the cross section of the interaction. σ is given as $\sigma = \pi \cdot (r_1 + r_2)^2$. r_1 and r_2 are the radii of the two particles. As one is an electron, it is approximated as $r_1 = 0$. r_2 is approximated as the radius of the argon atom of 106pm [18]. n is the particle density and defined as

$$n = \frac{p}{k \cdot T} \tag{4.6}$$

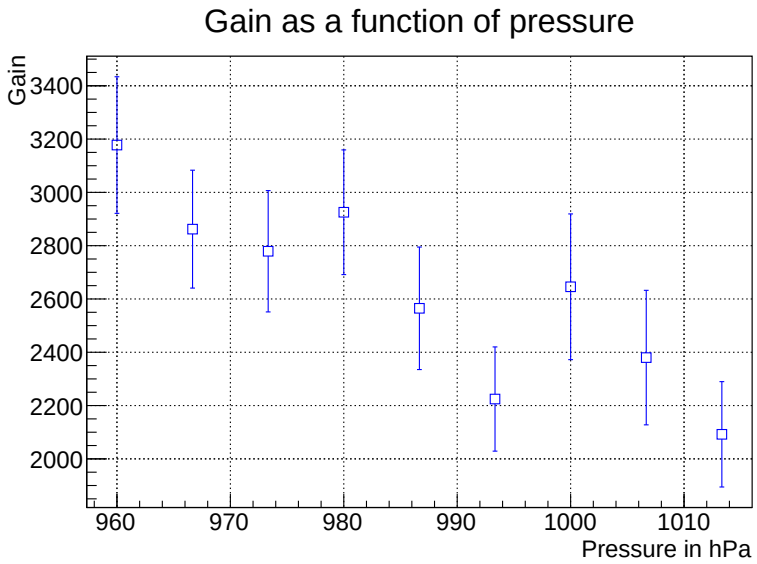

Figure 4.35: Gain for the triple layer GEM setup used in CMS under variation of pressure.

where k is the Boltzmann constant.

If 4.6 is inserted into 4.5, the mean free path can be calculated. At standard conditions, this results in about 2.5μm.

If each of these collisions was an ionizing collision, about 25 electrons would be expected to be generated while the initial electron travels trough the foil (the foil has a thickness of 60 µm). However, since not all collisions are ionizing and as this is a very simplified approach, this number is only a rough estimate.

For a λ of 2.5 µm and an electric field strength inside the hole of 55 kV cm^{-1} the electron will have an energy of 13.7 eV at the next collision. This is less than the ionization potential of the main gas mixture components listed in table 4.1. Therefore it should be beneficial to increase the mean free path to allow for more ionizing collisions.

The simulations are carried out for pressures in the range of 720 Torr (960 hPa) to 760 Torr (1013 hPa).

As can be seen in figure 4.35, the effective gain decreases with higher pressures due to the effects described above.

The transparency, temporal and spacial resolutions show no abnormalities (Appendix A: Figure A.9).

Temperature

Varying the temperature should have an opposite effect compared to the variation of pressure. It also changes the mean free path of the electron in the gas, following the relation in 4.5 and 4.6.

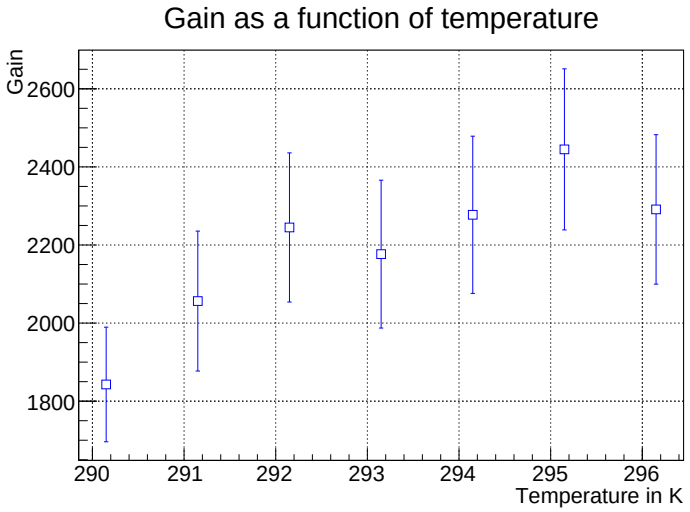

Figure 4.36: Gain for the triple layer GEM setup used in CMS under the variation of temperature.

In figure 4.36, the expected relation of gain to temperature can be seen. The nominal temperature at which the CMS GEM detectors will be operated is 297 K. The transparency, spacial and temporal distributions do not depend on the temperature of the gas inside the chamber (Appendix A figure A.10).

4.3.2 Real CMS GEM stack

The triple layer Single mask GEM stack with bottom orientation is also simulated. In addition, the rim is now removed because it is suspected that this is closer to reality as mentioned above in the single layer simulations.
In figure 4.37, the gain of the triple layer GEM is shown without rims around the holes in the single mask bottom configuration. Within the error this measurement is in accordance with the triple layer GEM double mask setup with rim that is also shown. This result was also obtained when simulating the single layer single mask GEM without a rim. This verifies that single layer results can be extrapolated to triple layer studies.
The spacial and the temporal resolutions (Appendix A figure A.8) show no significant difference compared to the triple layer double mask with rim results.

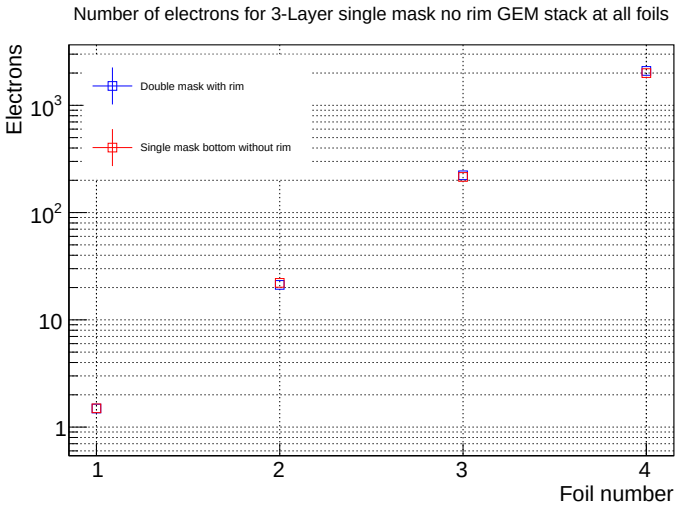

Figure 4.37: Gain for the triple layer single mask bottom no rim setup (red) compared to the double mask triple layer setup shown in figure 4.33.

4.4 Full Muon Simulation

Avalanches produced by the ionization of the gas by a muon crossing the detector are also computed to compare them to the single electron results.
In order to perform this, 186 muons are simulated fully. Each of the 186 muons created 20.15 ± 0.36 primary electrons on average.
Since each muon is set to travel trough the chamber vertically, it travels 7 mm inside the detector. Therefore a muon creates one primary electron every 0.347 ± 0.006 mm. This is on the order of observed creations of primary electrons described in [20].[2]
The primary electrons which later make up most of the avalanche are produced inside the first 3 mm drift gap (see figure 2.3). These are 8.64 ± 0.15 out of all produced primary electrons.
In figure 4.38, the temporal and the spacial resolutions of the chamber for a complete muon simulation are shown. For the temporal resolution the values that are noted in the histogram are the standard deviations of all 186 muon events. The Gaussian fit produces a standard deviation of 11.8 ± 3.24 ns. For the spacial distribution on the right, the endpoints of all electrons are shown. The mean is compatible with 0. Here it is evident that the previously chosen *sensor* area of 2×2 mm^2 is sufficient because even for the biggest and most spread out avalanche (the muon avalanche) all electrons within 5σ are included.

[2] As described before, the number of secondary electrons produced does not match the literature

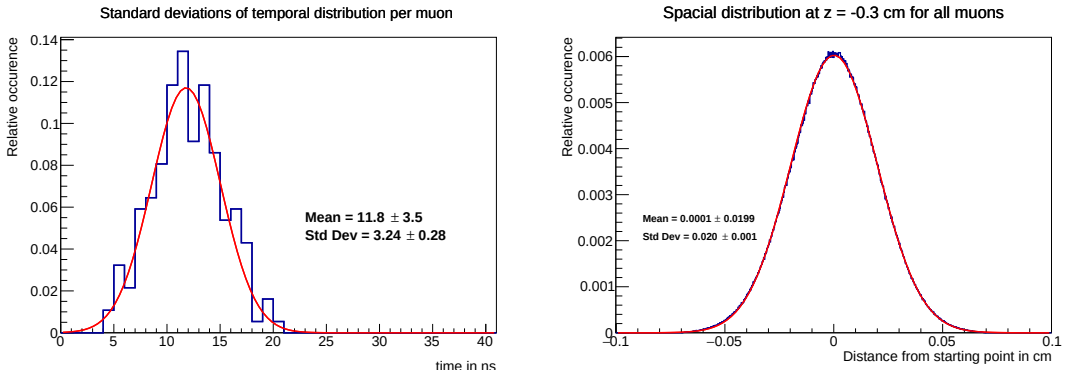

(a) Temporal resolution

(b) Spacial resolution

Figure 4.38: Temporal and spacial resolution at the readout board for the triple layer default setup GEM stack with Gaussian fits.

It is important to note that the spacial spread of the full muon simulation does not exceed that of the single electron triple layer simulation. This would however change if the muon was not set to travel through the chamber only in the z-direction.

Chapter 5

Conclusion and Outlook

The GEM simulation has revealed to be a powerful tool to understand the behavior of these kinds of detectors. It was shown that it is well possible to simulate nearly arbitrary GEM setups by varying many different parameters that are discussed in this thesis.
This thesis is mostly focused on a single layer GEM setup and a setup representing the CMS GEM detectors. The programs written for this thesis can however easily be adapted for other GEM setups.
The variation of the gas mixture inside the chamber has shown important results. When varying the gas mixture, there are several factors that influence the signals of the GEM, like the electron capture, the ionization potential and others. Due to the interference of different effects it was sometimes difficult to formulate a conclusive analysis of the simulation results. A small addition of a gas with a low ionization potential has shown positive effects on the gain of the chamber. O_2 and H_2O were tested as examples. It was shown that a small amount of air in the chamber is not significantly impacting the signals of the GEM. The program written for this thesis provides a versatile tool to simulate different gases in the future.
Another part of this thesis is the influence of the foil geometry on the GEM signals. The setup described in [1] was found to yield the highest gain and best overall results. Since the GEM is such a flexible detector in respect to its geometry, many more parameters can be analyzed in the future, like the influence of the spacing of the foils.
Simulations were also done to study the influence of environmental parameters on the signals of the GEM. These show the expected dependencies of the rising gain of the GEM for higher temperatures and lower pressures.
Finally the muon was simulated fully and compared to the previous results. A time resolution of 12 ns was found for the muon avalanche.
Nevertheless, this simulation offers a lot of opportunities beyond the scope of this

thesis. In the future, for example, a magnetic field could be taken into account as it is present in the environment of the CMS detector where the GEM chambers will be installed.
Furthermore, the drift field strength was not varied, but might have an impact on the overall performance of the detector (as described in [2]).
There is also the option to add a simulation of readout electronics with `Garfield++`, which was not investigated in this thesis.
Of course, all studies performed for the single layer setup could be done for the triple layer setup to confirm the results and possibly get more accurate findings.
The discrepancies between the simulation and the real experiment should be further investigated. Several attempts were made to find the cause of the discrepancies. It was tried to calculate the δ electron transport directly in `Garfield++` rather than with `Heed`, the Townsend coefficient and the gas table were computed separately and not used from the `Magboltz` database, but the discrepancies were still found. These discrepancies were also found by [25] and [26]. The latter proposed a solution of fixing them with an adjusted penning transfer rate, however after doing this the penning transfer rate is no longer in agreement with [24].
In the future there might also be an option within `Garfield++` to simulate ions with the same accuracy as electrons, offering the opportunity of simulating ion induced avalanches. When this feature is introduced, this simulation could easily be expanded to include these ion interactions.
Overall, these microscopic simulations give a good insight into the complex processes within a GEM.

Appendix A

Additional Plots

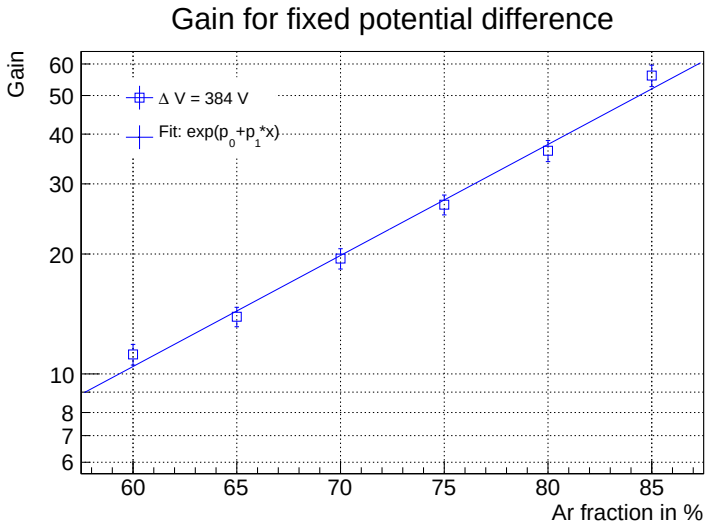

Figure A.1: Exponential relation of gain to argon fraction for fixed $\Delta V = 384\,V$.

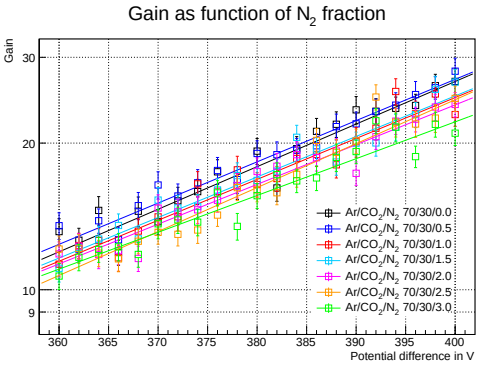

Figure A.2: Gain for all simulated additions of N_2.

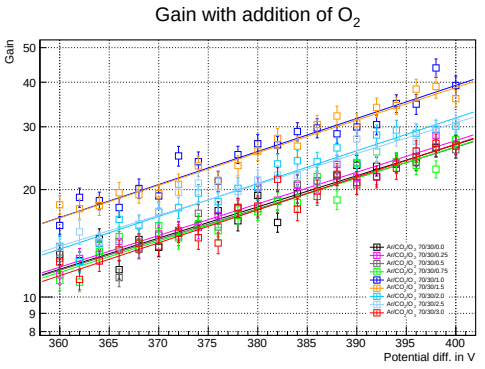

(a) Gain of all data points

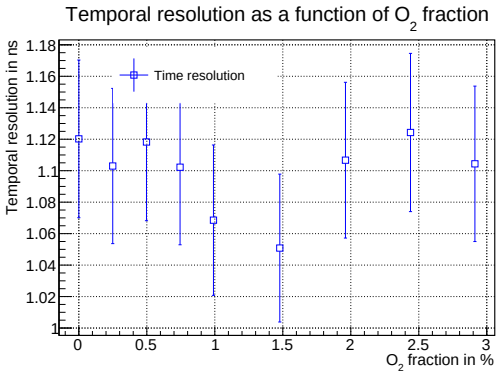

(b) Temporal resolution

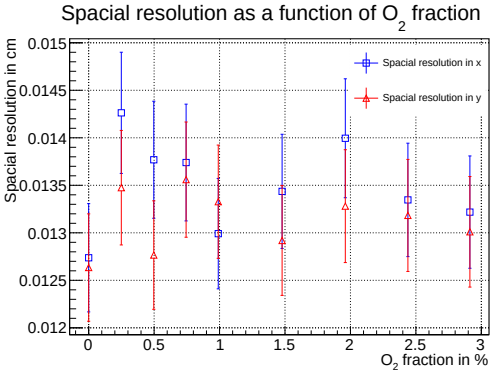

(c) Spacial resolution

Figure A.3: Additional plots for addition of O_2.

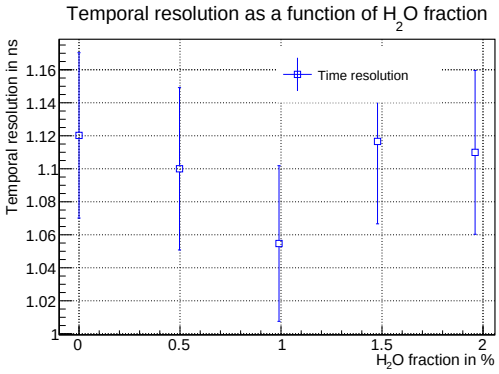

(a) Temporal resolution

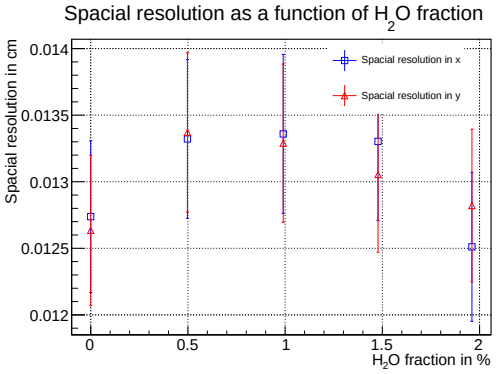

(b) Spacial resolution

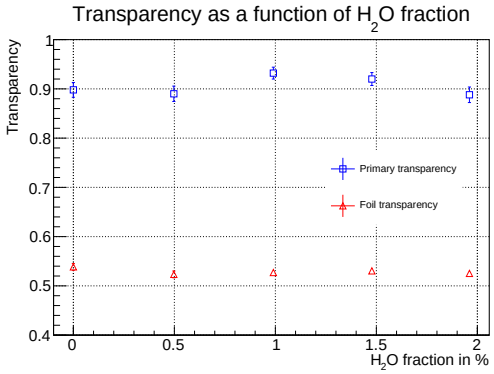

(c) Transparency

Figure A.4: Additional plots for addition of H_2O.

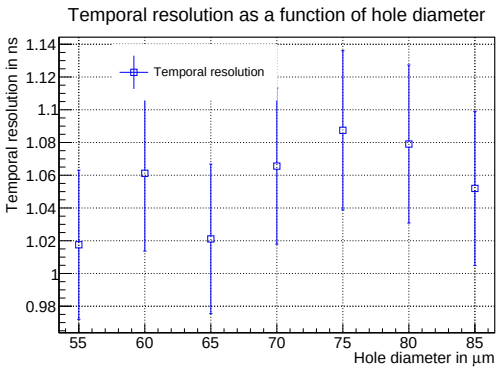

(a) Temporal resolution

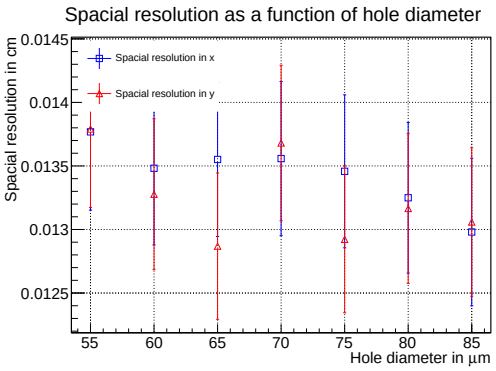

(b) Spacial resolution

Figure A.5: Additional plots for variation of the outer hole diameter

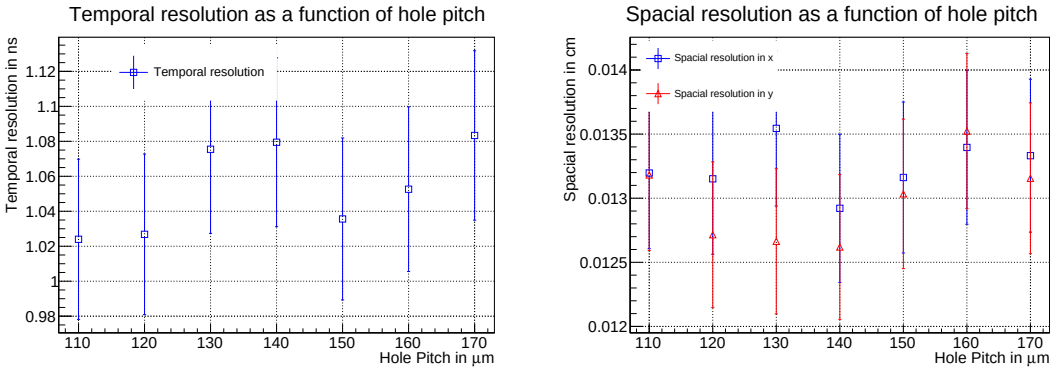

(a) Temporal resolution (b) Spacial resolution

Figure A.6: Additional plots for variation of the hole pitch

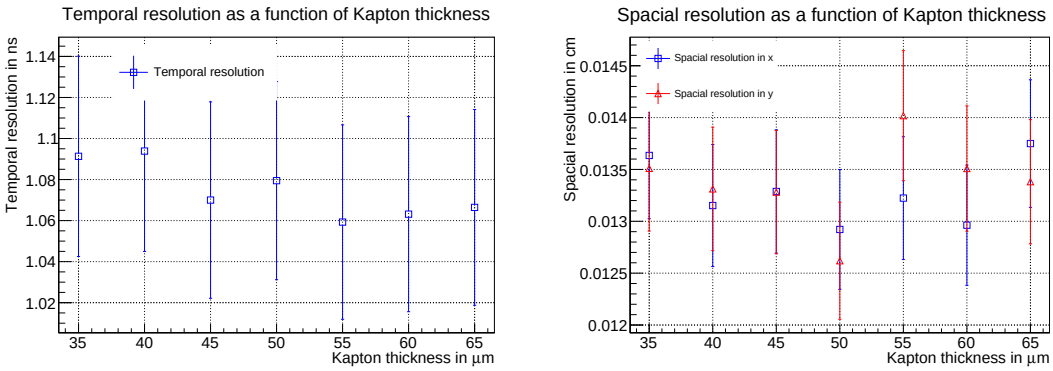

(a) Temporal resolution (b) Spacial resolution

Figure A.7: Additional plots for variation of the Kapton thickness

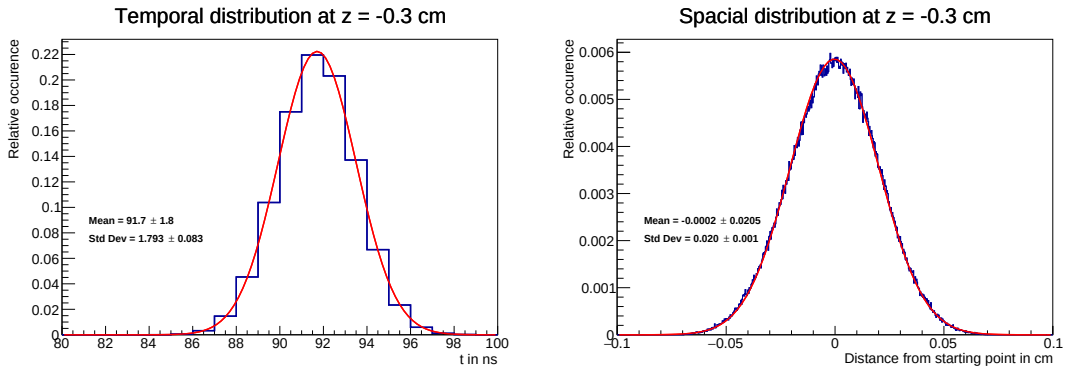

(a) Temporal resolution (b) Spacial resolution

Figure A.8: Additional plots for the triple layer no rim single mask bottom setup

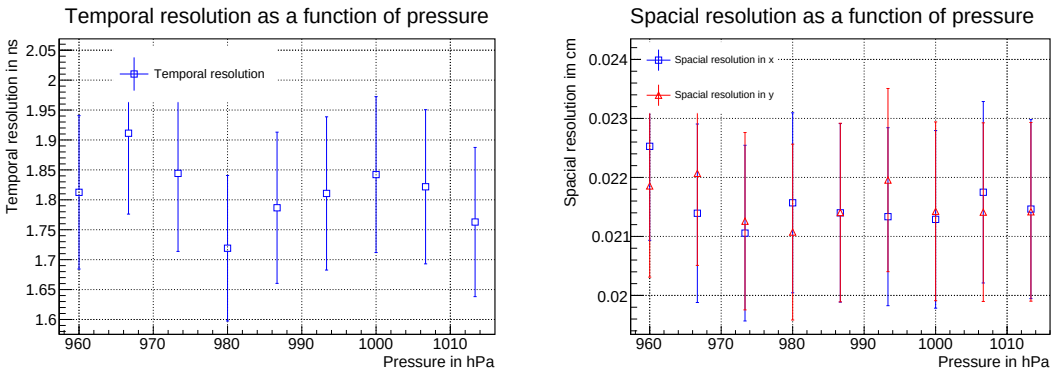

(a) Temporal resolution (b) Spacial resolution

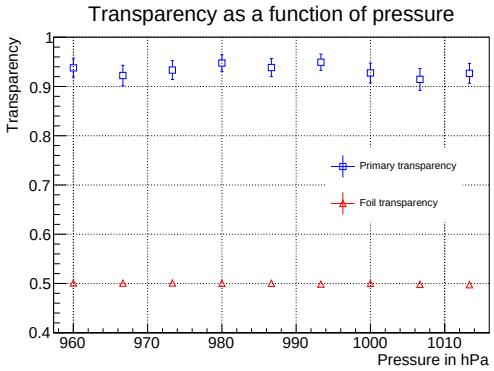

(c) Transparency

Figure A.9: Additional plots for pressure variation

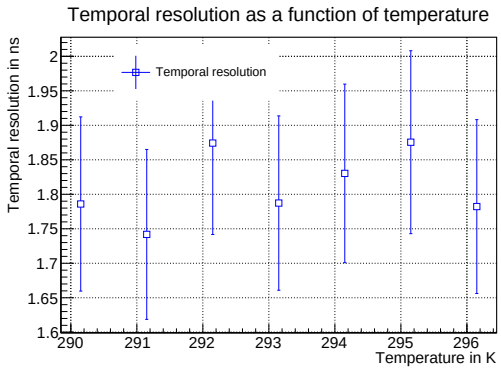

(a) Temporal resolution

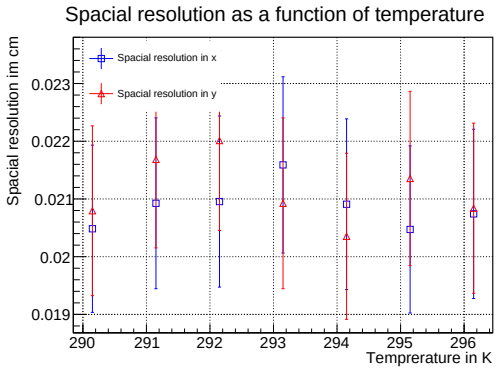

(b) Spacial resolution

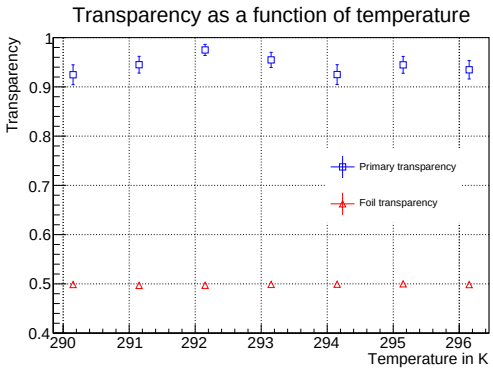

(c) Transparency

Figure A.10: Additional plots for temperature variation

Bibliography

[1] CMS Collaboration, *CMS Technical Design Report for the Muon Endcap GEM Upgrade*, CERN-LHCC-2015-012, 2015

[2] Fabio Sauli, *The gas electron multiplier (GEM): Operating principles and applications*, Nucl.Instrum.Meth. A805 2-24, 2016

[3] H. Geiger and W. Müller, *Das Elektronenzählrohr*, Physikalische Zeitschrift, 29: 839-841, 1928

[4] RD51 Collaboration, *Modeling the GEM E-field using finite elements*, RD51 Simulation School

[5] David Roylance, *Finite Element Analysis*, 2001, `https://ocw.mit.edu/courses/materials-science-and-engineering/3-11-mechanics-of-materials-fall-1999/modules/MIT3_11F99_fea.pdf` [Accessed 20.06.2018]

[6] Ansys, Ansys simulation software, `https://www.ansys.com/`

[7] Rob Veenhof et al., *Garfield++ Toolkit*, `http://garfieldpp.web.cern.ch/garfieldpp/` [Accessed 28.06.2018]

[8] Steve Biagi, *Magboltz - transport of electrons in gas mixtures*, `http://magboltz.web.cern.ch/magboltz/` [Accessed 28.06.2018]

[9] Igor Smirnov, *Modeling of ionization produced by fast charged particles in gases* `http://ismirnov.web.cern.ch/ismirnov/heed` [Accessed 28.06.2018]

[10] Anna Becker, *Analysis of the Temporal and Spacial Signal Propagation of a Triple GEM Detector*, 2018

[11] David Bolton, *The Computation of Equivalent Potential Temperature*, Monthly weather review; Vol. 108, 1979

[12] National Institute of Standard and Technology, `https://webbook.nist.gov` [Accessed 09.07.2018]

[13] R. K. Asundi et al., *Electron Attachment and Ionization in Oxygen, Carbon Monoxide and Carbon Dioxide*, Proc.Phys.Soc.82.967, 1963

[14] O. J. Orient, S.K. Srivastava, *Production of O- from CO_2 by dissociative electron attachment*, Chemical Physics Letters, Volume 96, Issue 6, 1983

[15] T. Zhao et al., *A study of electron drift velocity in $ArCO_2$ and $ArCO_2CF_4$ gas mixtures*, Nucl.Instrum.Meth Volume 340, Issue 3, 1994

[16] A. Andronic et al., *Drift velocity and gain in argon- and xenon-based mixtures*, Nucl.Instrum.Meth.A523:302-308, 2004

[17] J. A. Merlin, *GEM single-mask characterization and influence of the GEM foil orientation*, MPGD2017, 2017

[18] E. Clementi, D. L. Raimondi, *Atomic Screening Constants from SCF Functions*, The Journal of Chemical Physics 38, 2686, 1963

[19] CMS collaboration, *CMS, the Compact Muon Solenoid: Technical proposal*, CERN-LHCC-94-38, 1994

[20] A. Sharma, *Properties of some gas mixtures used in tracking detectors*, SLAC-JOURNAL-ICFA-16-3, July 1998

[21] H. Schindler, *Garfield++ User Guide*, Garfield++, 2017

[22] F. Simon et al., *Triple GEM detectors for the forward tracker in STAR*, 10.1109/NSSMIC.2007.4436321, 2007

[23] PHY251, `http://felix.physics.sunysb.edu/~allen/252/PHY251_Geiger.html` [Accessed 09.07.2018]

[24] Ö. Sahin et al., *High-precision gas gain and energy transfer measurements in Ar–CO_2 mixtures*, Nucl.Instrum.Meth. A768 (2014) 104-111, 2014

[25] S. Swain et al., *A simulation study for designed triple GEM detector at IOP*, Bose Institute Conference, 2017

[26] Ö. Sahin, *Penning Transfers*, 2nd RD51 Collaboration Meeting Paris, 2008

[27] J. A. Merlin *Study of long-term sustained operation of gaseous detectors for the high rate environment in CMS*, CERN-THESIS-2016-041, 2016

Eidesstattliche Versicherung

Name, Vorname	Matrikelnummer

Ich versichere hiermit an Eides Statt, dass ich die vorliegende Bachelorarbeit mit dem Titel

Microscopic Simulation of GEM Signals

selbständig und ohne unzulässige fremde Hilfe erbracht habe. Ich habe keine anderen als die angegebenen Quellen und Hilfsmittel benutzt. Für den Fall, dass die Arbeit zusätzlich auf einem Datenträger eingereicht wird, erkläre ich, dass die schriftliche und die elektronische Form vollständig übereinstimmen. Die Arbeit hat in gleicher oder ähnlicher Form noch keiner Prüfungsbehörde vorgelegen.

Ort, Datum	Unterschrift